A CO-multilayer outer atmosphere for eight evolved stars revealed with VLTI/AMBER

M. Hadjara, P. Cruzalèbes, C Nitschelm, X. Chen, E Michael, Edmundo Moreno

Monthly Notices of the ROYAL ASTRONOMICAL SOCIETY

MNRAS **489,** 2595–2614 (2019) doi:10.1093/mnras/stz2240

A CO-multilayer outer atmosphere for eight evolved stars revealed with VLTI/AMBER

M. Hadjara,[1,2,3★] P. Cruzalèbes,[4★] C. Nitschelm,[5] X. Chen,[6] E. A. Michael[1] and E. Moreno[1]

[1]*Radio Astronomical Instrumentation Group (RAIG), Terahertz- and Astro-Photonics Laboratory, Departamento de Ingeniería Eléctrica, Universidad de Chile, Avenida Tupper 2007, Santiago, Chile*
[2]*Instituto de Astronomía, Universidad Católica del Norte, Av. Angamos 0610 Antofagasta, Chile*
[3]*Centre de Recherche en Astronomie, Astrophysique et Géophysique (CRAAG), Route de l'Observatoire, BP 63, Bouzareah, 16340, Alger, Algeria*
[4]*Université Côte d'Azur (UCA), Centre National de la Recherche Scientifique (CNRS), Observatoire de la Côte d'Azur (OCA), Laboratoire J. L. Lagrange, UMR 7293,Campus Valrose, 06108 Nice Cedex 2, France*
[5]*Centro de Astronomía (CITEVA), Universidad de Antofagasta, Avenida Angamos 601, Antofagasta 1270300, Chile*
[6]*Optical Interferometry Group, Shanghai Astronomical Observatory(SHAO), Chinese Academy Sciences(CAS) , Shanghai, 200030, China*

Accepted 2019 August 3. Received 2019 August 3; in original form 2019 May 28

ABSTRACT

We determine the physical parameters of the outer atmosphere of a sample of eight evolved stars, including the red supergiant α Scorpii, the red giant branch stars α Bootis and γ Crucis, the K giant λ Velorum, the normal M giants BK Virginis and SW Virginis, and the Mira star W Hydrae (in two different luminosity phases) by spatially resolving the stars in the individual carbon monoxide (CO) first overtone lines. We used the Astronomical Multi-BEam combineR (AMBER) instrument at the Very Large Telescope Interferometer (VLTI), in high-resolution mode ($\lambda/\Delta\lambda \approx 12\,000$) between 2.28 and 2.31 μm in the K band. The maximal angular resolution is 10 mas, obtained using a triplet telescope configuration, with baselines from 7 to 48 m. By using a numerical model of a molecular atmosphere in a spherical shells (MOLsphere), called PAMPERO (an acronym for the 'physical approach of molecular photospheric ejection at high angular resolution for evolved stars'), we add multiple extended CO layers above the photospheric MARCS model at an adequate spatial resolution. We use the differential visibilities and the spectrum to estimate the size (R) of the CO MOLsphere, its column density ($N_{\rm CO}$) and temperature ($T_{\rm mol}$) distributions along the stellar radius. The combining of the $\chi 2$ minimization and a fine grid approach for uncertainty analysis leads to reasonable $N_{\rm CO}$ and $T_{\rm mol}$ distributions along the stellar radius of the MOLsphere.

Key words: methods: numerical – methods: observational – techniques: high angular resolution – stars: AGB and post-AGB – stars: atmospheres – stars: fundamental parameters.

1 INTRODUCTION

The red giant branch (RGB) and asymptotic giant branch (AGB) house giant cool evolved stars in late evolutionary stages, particularly of spectral types K and M with low and intermediate masses ($0.8 \lesssim M/{\rm M}_\odot \lesssim 8$). During their lifetime, the latter can lose up to 30 per cent of their initial mass (Wachter et al. 2002), which means that they play a crucial role in the chemical evolution of the galaxy. They enrich the interstellar medium (ISM) by dredging their nuclear-processed material up to the surface before expelling it into the circumstellar environment, while affecting their evolutionary journey at the same time. These features make these stars one of the most important components of the cosmic mechanism of matter recycling.

According to the amplitudes of their variability, the K and M giant stars can be classified into two principal subtypes:

(i) Mira-type stars, which are in the AGB phase with light amplitudes ranging from 2.5 to 11 in V magnitude and a pronounced periodicity of 80–1000 d;

(ii) semiregular or irregular variable K–M giant stars (simply designated by the term 'normal K–M giant stars' in this paper), which have amplitudes varying from several hundredths to several magnitudes (usually 1–2 in V magnitude) and an unclear periodicity.

★ E-mail: massinissa.hadjara@gmail.com (MH); Pierre.Cruzalebes@oca.eu (PC)

According to the recent list of the General Catalogue of Variable Stars (GCVS) version 5.1 (Samus' et al. 2017),[1] we count 2271 Mira stars and 2235 normal K–M giants (denoted as L, LB, SRA, SRB, SRC and SRD in the catalogue) that are currently clearly identified in the Galaxy. Even though the numbers are similar, the normal K–M giant stars remain relatively less studied than the Mira stars. Indeed, the Mira-type stars in the AGB phase, which show variability amplitudes much greater than the normal K–M giants, are easier to detect and study. If we focus only on the normal M giants in the AGB phase and compare their mass-loss rates ($\dot{M}$) with those of Mira stars, we observe that they are nearly the same. Normal K–M giants have $\dot{M}$ between 10^{-8} and 10^{-6} $M_\odot$ yr^{-1} with an expansion velocity ($v_{\rm exp}$) from 3 to 15 km s^{-1} (e.g. Knapp et al. 1998; González Delgado et al. 2003; Winters et al. 2003; Mondal & Chandrasekhar 2005; De Beck et al. 2010), which means a total mass loss of 0.1 $M_\odot$ during their full AGB lifetime (Origlia et al. 2014). For the Mira stars, $\dot{M} = 10^{-8}$–10^{-6} $M_\odot$ yr^{-1} with $v_{\rm exp}$ = 3–20 km s^{-1} (e.g. Knapp et al. 1998; Winters et al. 2003; Mondal & Chandrasekhar 2005). It is also important to note that the mass-loss rates of some Mira stars with substantial dust shells can reach 10^{-5} $M_\odot$ yr^{-1} and more (Höfner & Olofsson 2018, and references therein). Red giant stars near the RGB tip may lose more than 10^{-6} $M_\odot$ yr^{-1} (Ita et al. 2007; Origlia et al. 2007, 2010). Mass loss chemically feeds the circumstellar environment (CSE) of AGB stars as well as the ISM. The chemical composition of the ejected material is determined by the carbon/oxygen ratio (C/O; e.g. Woolf 1973), from which we can classify those stars into three different types, as follows; more details about the evolved stars, their CSE and the most recent works of this field have been summarized by Li et al. (2016), Di Criscienzo et al. (2016) and Habing (1996).

(i) Oxygen-rich (O-rich) stars. With C/O < 1, the manufactured/ejected carbon by the star will quickly bond with oxygen (if temperature and pressure permit) to form very stable carbon monoxide (CO) molecules. The remaining oxygen will form oxygen-rich molecules (such as silicates and oxides) and particles (such as aluminium monoxide; e.g. Ita et al. 2007; De Beck et al. 2017).

(ii) Carbon-rich (C-rich) stars. With C/O > 1, the excess of carbon will produce dust of silicon carbide and graphites (Guha Niyogi, Speck & Volk 2011). Note that in their sample of 10 O-rich and four C-rich giants,Cruzalèbes et al. (2015) observed more predominant CSE asymmetry for the C-rich stars than for the O-rich stars.

(iii) S-type stars. Where C/O ≈ 1, this is traditionally considered as a transitional evolutionary step between O-rich and C-rich stars. Note that the abundances of other elements such as lithium and zirconium of O-rich stars are affected by s-process enrichment and hot-bottom burning (García-Hernández et al. 2007).

In the early 1980s, it was argued that it might be possible to distinguish an extramolecular layer from the hot chromosphere and the cool expanding wind, based on the CO 2–0 spectra of Mira stars (even though water vapour spectra had been observed on cool luminous stars since the early 1960s; see Tsuji 2006, and references therein). The indisputable evidence for the existence of an extended molecular envelope was first observed, using the speckle interferometry technique, by Labeyrie et al. (1977), on the Mira stars, o Ceti and R Leo, for which they measured angular diameters two times larger in the TiO absorption lines than in the continuum. Since then, several observations have confirmed the presence of these extramolecular layers around M giants in the AGB phase (Tsuji 2006; Arroyo-Torres et al. 2015, and references therein). Beside this, more recently, it has been demonstrated that the measured relative size ratio, of these evolved stars, in the continuum and in the absorption band heads of some oxygen-rich molecules (such as the silicates and oxides) can reach more than 50 per cent (Martí-Vidal et al. 2011;Wittkowski et al. 2016, and references therein). Thus, their size appears, at certain wavelengths, much larger than predicted by the classical stellar atmospheric and hydrostatic models (e.g. MARCS). This extended region of a few stellar radii (R_*), between the upper photosphere and the innermost part of the circumstellar envelope, where the stellar wind is supposed to take its energy and momentum, was named the MOLsphere by Tsuji (2006). The mechanism responsible for mass loss could be directly related to the physical process that generates the MOLsphere. The study of the MOLsphere is therefore very important in order to better understand the mass-loss phenomenon of red giant stars in general (Tsuji et al. 1997; Tsuji 2001; Perrin et al. 2004; Ohnaka 2004; Wittkowski et al. 2007; Chiavassa et al. 2010, 2011; Ohnaka et al. 2012; Ohnaka 2013; Arroyo-Torres et al. 2015; Wittkowski et al. 2016, 2017; Ohnaka, Hadjara & Maluenda Berna 2019).

Long-baseline spectro-interferometry in the near-infrared (NIR) is an observation tool that allows us to resolve and finely study the relatively optically thin and extended MOLspheres of K–M giants. Indeed, by using this technique with the Astronomical Multi-BEam combineR (AMBER) instrument at the Very Large Telescope Interferometer (VLTI), Ohnaka et al. (2012) were able to resolve the CO present in the MOLsphere of a rich panel of K–M giant stars and to determine their sizes, temperature and column density distributions (using a two-layer model), and then to conclude on the MOLsphere's behaviour. Thus, to extend this work, we decided to use the same instrument to study different types of K–M giants: the irregular variable red supergiant (RSG) α Scorpii (α Sco), the RGB star with low variability α Bootis (α Boo), the normal eruptive semivariable M giant γ Crucis (γ Cru), the normal slow irregular K giant λ Velorum (λ Vel), the semivariable M giants BK Virginis (BK Vir) and SW Virginis (SW Vir) , and the Mira star W Hydrae (W Hya). These observations were at post-minimum light for the observation of 2014 February 11 and at pre-maximum light for the observation of 2014 April 22, with phases of 0.59 and 0.77, respectively, according to Ohnaka, Weigelt & Hofmann (2016, 2017b), using the light curves of the American Association of Variable Star Observers (AAVSO).

In this paper, we study and analyse the results obtained by the VLTI/AMBER at high spectral resolution in the K band. We use our numerical model PAMPERO (an acronym for the 'physical approach of molecular photospheric ejection at high angular resolution for evolved stars') to constrain the physical properties of CO outer layers from the observed flux and visibilities of our target, and to determine the distributions of the CO column density $N_{\rm CO}$ and the temperature $T_{\rm mol}$ along the stellar radius. We validate our model by using already published data for α Boo (Ohnaka & Morales Marín 2018), BK Vir (Ohnaka et al. 2012) and SW Vir (Ohnaka et al. 2019), and new data for α Sco, γ Cru, λ Vel and W Hya (for two different phases of activity). In Section 2, we present the observations and the data reduction. In Section 3, we analyse and discuss the final reduced data. In Section 4, we describe the model used. In Section 5, we deduce the relevant stellar parameters

[1]Note that there are many stars in the GCVS version 5 with an unknown spectral type and that Lebzelter, Kerschbaum & Hron (1995) found, for more than 40 per cent of the studied GCVS4 objects, that they are deduced from poor and sparse light curves.

of our targets and we discuss the results. Finally, we conclude in Section 6.

2 OBSERVATIONS AND DATA REDUCTION

Our sample of stars was observed with the VLTI/AMBER instrument (Petrov et al. 2007) with the Auxiliary Telescopes (ATs) triplets B2-C1-D0 (16-32-48m) for 2009 April 16, B2-C1-D0 (10-20-30m) for 2014 February 11 and A1-B2-C1 (7-10-15m) for 2014 April 22. In order to observe the $^{12}C^{16}O$ (hereafter simply CO) first overtone lines near the 2–0 band head at 2.294 μm, the observations have been carried out using the high spectral resolution mode of AMBER ($\lambda/\Delta\lambda \approx 12\,000$) in the *K* band (HR_K) between 2.28 and 2.31 μm. Because of the high brightness of the K–M giants, observed with good weather conditions (seeing of 0.7–1.2 arcmin), the low-contrast fringes (for each of the three baselines) were detected without the use of the VLTI fringe tracker FINITO (Mérand et al. 2012). So, the measurements have been performed with a detector integration time (DIT) of 0.12 s and 500 exposures. The Sun-like star α Cen A (HD 128620) of spectral type G2.0 V (Léger et al. 2015) was used as the interferometric and spectroscopic calibrator for all our science targets, except for BK Vir. For this specific target, the interferometric calibrator β Crv could not be used as a spectroscopic calibrator. In this case, we used the method proposed by Ohnaka et al. (2012) (further explanations below). Table 1 provides the observation log of our sample of targets with the corresponding (u, v) coverage shown in Fig. 1.

In Fig. 1, we adopt a colour for each star (and for W Hya for each phase). We keep and use this colour code in each figure that follows in this paper.

Because of the spectro-interferometric technology of AMBER, we were able to measure, in addition to the spectrum, the following quantities related to the complex spatial Fourier transform of the brightness of our targets.

Table 1. VLTI/AMBER observations, with AT Triplets B2-C1-D0 (for the nights of 2009 April 16 and 2014 February 11) and A1-B2-C1 (for the night of 2014 April 22), of our sample of targets with details on the dates, times and baseline triplets. The calibrators are α Cen A and β Crv.

Object	Date and time	Baseline length $B_{\rm proj}$ (m)	Baseline PA PA (°)
β Crv	2009-04-16T03:07	16,32,48	73,73,73
BK Vir	2009-04-16T03:47	16,32,48	68,68,68
α Cen A	2014-02-11T05:06	10,20,30	165,165,165
γ Cru	2014-02-11T05:24	10,21,31	08,08,08
α Cen A	2014-02-11T05:41	10,20,30	171,171,171
SW Vir	2014-02-11T06:37	10,20,29	14,14,14
α Cen A	2014-02-11T06:56	10,20,31	03,03,03
λ Vel	2014-02-11T07:13	09,19,28	45,45,45
α Cen A	2014-02-11T07:30	10,20,30	08,09,09
α Boo	2014-02-11T07:49	07,15,22	21,21,21
α Cen A	2014-02-11T00:17	10,20,30	14,14,14
W Hya	2014-02-11T08:28	11,23,34	21,21,21
W Hya	2014-04-22T00:38	07,11,12	03,85,120
α Cen A	2014-04-22T00:58	07,10,16	127,73,96
W Hya	2014-04-22T01:16	08,11,13	07,91,129
α Cen A	2014-04-22T01:34	08,10,16	140,80,106
α Cen A	2014-04-22T01:51	08,10,16	150,86,115
α Cen A	2014-04-22T01:58	09,10,16	155,88,119
α Sco	2014-04-22T02:13	05,11,11	179,76,101
α Cen A	2014-04-22T02:30	09,10,16	163,94,126

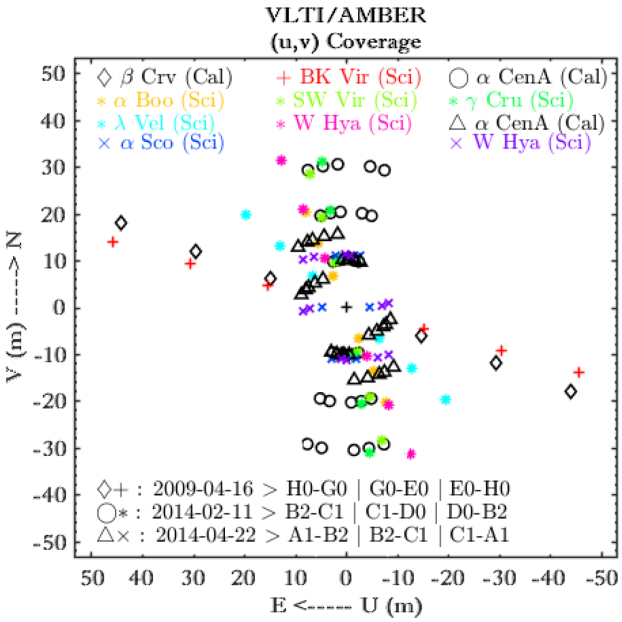

Figure 1. Baselines and the corresponding (u, v) coverage of VLTI/AMBER observations of our sample of eight K–M giants. Earth-rotation synthesis spanned over ∼1.1 h per night. The science targets are represented by colour symbols while the calibrators (α Cen A and β Crv) are denoted by black symbols.

(i) The differential visibility amplitude informs us about the shape and the size of the target on several wavelengths between 2.28 and 2.31 μm.

(ii) The differential phase ($\phi_{\rm diff}$) is related to the photocentre displacement at the first order (Jankov et al. 2001) and informs us about the asymmetry as well as the kinematic behaviour of the observed upper and outer stellar layers (photosphere, MOLsphere, CSE, etc.).

(iii) The closure phase (Ψ) is the sum of all the $\phi_{\rm diff}$ of each baseline. For a point-symmetric object, its value is always equal to zero or π. $\Psi \neq 0$ and $\Psi \neq \pi$ mean that the object is asymmetric but the inverse is not always true. An unresolved or partially resolved object has a $\Psi = 0$, for example.

Our AMBER data have been reduced using version 3.0.9 of the AMDLIB[2] software (Tatulli et al. 2007; Chelli, Utrera & Duvert 2009). We adopted a standard frame selection based on the fringe signal-to-noise (S/N) ratio (Millour et al. 2007) and we kept the 80 per cent best-calibrated frames later using the same appropriate reduction methods as those used by Ohnaka et al. (2009, 2012, 2013), including the error estimation of the calibrated visibilities, $\phi_{\rm diff}$ and Ψ. Indeed, as a result of these reduction tools, we have performed a wavelength calibration (with a spectral uncertainty of 1.7×10^{-5} μm or ∼2 km s^{-1}). We used the identified calibrator's (α Cen A and β Crv) telluric lines from a sample of the atmospheric transmission spectrum, which were measured at Kitt Peak National Observatory[3] and were convolved in order to match with the spectral resolution of AMBER's observing mode. Then we converted the wavelength scale to the laboratory frame using heliocentric velocities of -24.7 ± 0.4 km s^{-1} for α CenA and

[2]Available at http://www.jmmc.fr/data_processing_amber.htm.
[3]http://www.eso.org/sci/facilities/paranal/ instruments/isaac/tools/spectra/atmos_S_K.fits.

Table 2. Heliocentric velocities and radial velocities of our sample of targets (science and calibrators) for each date.

Object	Heliocentric velocity[a] ($\mathrm{km\,s^{-1}}$)	Radial velocity[b] ($\mathrm{km\,s^{-1}}$)
Night: 2009 April 16		
β Crv	-7.60 ± 0.10	-3.83
BK Vir	16.53 ± 0.35	-10.06
Night: 2014 February 11		
α Cen A	-24.7 ± 0.4	$\sim$22.17
γ Cru	21.0 ± 0.6	18.20
SW Vir	-15.0 ± 4.4	25.32
λ Vel	17.6 ± 0.3	4.60
α Boo	-5.2 ± 0.1	23.13
W Hya	42.3 ± 3.0	25.30
Night: 2014 April 22		
α Cen A	-24.7 ± 0.4	$\sim$10.65
W Hya	42.3 ± 3.0	-2.18
α Sco	-3.5 ± 0.8	18.88

[a]Gontcharov (2006).
[b]IRAF (RVCORRECT module).

of -7.6 ± 0.1 km s^{-1} for β Crv, both measured by Gontcharov (2006), without forgetting the Sun–Earth radial velocity, which takes into account the observation's time and location, from the IRAF[4] module RVCORRECT, in order to convert the observed velocity to the heliocentric frame. For the calibration of our interferometric data, we adopted the uniform-disc diameter of 8.31 ± 0.02 mas (Kervella et al. 2003) for α Cen A.[5] The uniform-disc diameter that we use for β Crv is of 3.27 ± 0.36 mas, from the JMMC Stellar Diameters Catalogue (JSDC; Bourges et al. 2017), whose the value is close to that of 3.40 ± 0.30 mas (Richichi & Percheron 2005). Table 2 summarizes all heliocentric velocities and radial velocities for our sample of targets (science and calibrators).

We also use α Cen A for the spectral calibration but, because it is a solar-type star (G2 V), we have an excess of CO absorption lines that must be removed. For that purpose, we use the method of Ohnaka et al. (2012, 2013), which consists first of calibrating α Cen A's spectrum with the spectrum of the Sun. The solar flux (observed by Wallace & Hinkle 1996) is set at the same spectral resolution and wavelength range as our AMBER data. However, for β Crv, for which no similar spectrum at the K band and in high resolution is available in the literature, we first perform (as Ohnaka et al. 2012) an auto-spectral calibration using the theoretical spectrum from the stellar atmosphere model MARCS (Gustafsson et al. 2008, where $T_{\mathrm{eff}}/\log g/M_{\star}/v_{\mathrm{micro}}/[\mathrm{Fe/H}] = 2800/0.0/0.5/2.0/+0.0$ with a moderately CN-cycled composition), before calibrating the spectrum of BK Vir.

3 DATA INTERPRETATION

This section concerns only the new data (i.e. γ Cru, λ Vel, α Sco and W Hya). For BK Vir, α Boo and SW Vir, data interpretation is well discussed by Ohnaka et al. (2012), Ohnaka & Morales Marín (2018) and Ohnaka et al. (2019), respectively. For practical reasons, all the figures for this section are gathered in Appendix A.

Figs A1–A5 show the observed visibilities, ϕ_{diff}, Ψ, and spectrum of γ Cru (Fig. A1), λ Vel (Fig. A2), α Sco (Fig. A3), W Hya for a phase of 0.59 (Fig. A4) and W Hya for an activity phase of 0.77 (Fig. A5). The signatures of the CO lines are clearly observable for all stars but even more for W Hya. Despite the short DIT of 0.12 s, the lowest visibility that could be measured in the CO lines is $\sim$0.1 for γ Cru (Fig. A1b), $\sim$0.5 for λ Vel (Fig. A2c), $\sim$0.3 for α Sco (Figs A3b and c) and $\sim$0.01 for W Hya (Figs A4c and A5c).

Panels (d) in Figs A1–A5 represent the uniform disc diameters, which were obtained from the respective observed visibilities. They show that the CO first overtone line diameters are 1–17 per cent larger (25–29 mas) than those in the continuum (24.8 mas) for γ Cru (Fig. A1d), 5–10 per cent larger (12–12.5 mas compared to 11.4 mas in the continuum) for λ Vel (Fig. A2d), 8–10 per cent larger (39.4–40 mas compared to 36.5 mas) for α Sco (Fig. A3d), 21–53 per cent larger (55–70 mas compared to 46.6 mas) for W Hya (post-minimum phase 0.59, Fig. A4d) and 38–72 per cent larger (56–70 mas compared to 40.7 mas) for W Hya (pre-maximum phase 0.77, Fig. A5d). Note that the uniform disc represent well the object's shape in the continuum, where the star looks bare without the MOLsphere (and where its fit is better with a reduced χ^2 between 0 and 2 for γ Cru, and between 0 and 0.5 for λ Vel and α Sco). However, the uniform disc does not represent at all well the object's shape for the Mira star, W Hya, in the continuum (with a reduced χ^2 of 0–35 at phase 0.59 and a very high value $\geq$35 at phase 0.77). The uniform-disc approach in the CO lines is worse, because of the detection of the MOLsphere at those lines (where the fit is poor with a reduced χ^2 value between 3 and 40 for γ Cru, between 1 and 7.5 for λ Vel, between 1 and 25.7 for α Sco, between 5 and 67 for W Hya at phase 0.59 and $\geq$50 for W Hya 0.77). So, the uniform disc's diameter (in the CO lines) can be considered only as a coarse estimation and especially for the Mira star W Hya.

Panels (e)–(h) in Figs A1–A3 show quasi-flat ϕ_{diff} and Ψ, which means a symmetry in the CO line-forming region, as in the continuum. Here, the star is detected without any MOLsphere, which means that γ Cru, λ Vel and α Sco seem to be point-symmetric objects. Figs A4(e)–(h) show $\Psi \neq 0$ and $\Psi \neq \pi$, which means that there is asymmetry in the CO line-forming region and that W Hya (with a phase of 0.59) seems to be an asymmetric object. The detection of non-zero ϕ_{diff} and non-zero/non-π Ψ (particularly clear on the 11.3-m baseline, with a peak of 134° at $\lambda = 2.294$ μm and 179° at $\lambda = 2.229$ μm), means that there is asymmetry in the CO line-forming region. Conversely, in the continuum, where the star is detected without any MOLsphere, W Hya (with a phase of 0.59) seems to be a point-symmetric object. This is the same for Figs A5(e)–(h), which show $\Psi \neq 0$ and $\Psi \neq \pi$ and asymmetry in the CO line-forming region, which means that W Hya (with a phase of 0.77) seems to remain an asymmetric object (but more than for a phase of 0.59).

By comparing the data on the diameter of W Hya's uniform disc (especially in the continuum), which were obtained from the observed visibilities, on both phases, we easily observe that the star's size is significantly larger on the post-minimum phase than on pre-maximum phase (as noted by Ohnaka et al. 2017b, by comparing two visibilities with the same baseline at different epochs).

For γ Cru and λ*Vel*, when we compare the observed visibilities of representative CO lines with their corresponding spectroscopic line centre, we do not observe any shift. However, for W Hya at the two observed phases, the minima of visibilities switch

[4]The Image Reduction and Analysis Facility (IRAF) is distributed by the National Optical Astronomy Observatories, which are operated by the Association of Universities for Research in Astronomy, Inc., under cooperative agreement with the National Science Foundation.
[5]The CHARM2 catalogue (Richichi, Percheron & Khristoforova 2005) confirmed the same angular diameter two years later.

randomly between the blue and red wings of the spectroscopic line. Ohnaka et al. (2009, 2011) interpreted these asymmetric visibilities as temporally variable inhomogeneous gas on the MOLsphere. According to the obvious wavelength shift of the visibilities with respect to the spectroscopic line centre, we suggest that the velocity amplitude of instantaneous inhomogeneous gas for γ Cru and λ Vel is zero, but that it is not negligible (around $\simeq 25\,\mathrm{km\,s^{-1}}$, which is the velocity resolution of AMBER in high spectral resolution mode) and highly random for W Hya (i.e. MOLspheric velocities of Mira stars that correspond to those found in the literature; e.g. Hinkle, Scharlach & Hall 1984; Bessell, Scholz & Wood 1996; Ireland, Scholz & Wood 2011).

4 MODELLING OF THE AMBER DATA

To interpret the AMBER observations of our sample of evolved stars, we used a spectro-interferometric multilayer MOLsphere model (described Section 4.2), which surrounds a photosphere with centre-to-limb intensity variations (CLV) profiles at each wavelength that we computed using Turbospectrum software (Alvarez & Plez 1998; Plez 2012), from MARCS stellar atmosphere models (Gustafsson et al. 2008) over the observed wavelength range using the CO line list of Goorvitch (1994). Each MARCS model[6] is specified by some stellar parameters that we should determine first: the effective temperature ($T_{\rm eff}$), surface gravity ($\log g$), micro-turbulent velocity ($v_{\rm micro}$), chemical composition and stellar mass ($M_\star$). In the following subsection, we describe the determination of these parameters.

4.1 Determination of stellar parameters

Most of the basic stellar parameters of our sample of evolved stars – the spectral type, variability type, magnitude, distance, angular diameter $\varnothing_\star$, effective temperature $T_{\rm eff}$, surface gravity $\log g$, mass $M_\star$, luminosity $L_\star$, micro-turbulent velocity $v_{\rm micro}$, metallicity [Fe/H] and ^{12}CO/^{13}CO ratio – are available in the literature and they are summarized in Table B1 (Appendix B). The 'Reference' line of Table B1 gives the main references from which the parameters' values were extracted for each star. Variability types and magnitudes values are taken from the GCVS version 5.1 (Samus' et al. 2017) for variable stars and from Ducati (2002) for other stars. All distance values are taken from van Leeuwen (2007) except for W Hya, whose distance values are taken from Knapp et al. (2003) (as was the case for Ohnaka et al. 2016, 2017b).

We deduce the stellar mass of W Hya by comparing its position ($\log(L_\star/\mathrm{L}_\odot)$, $\log(T_{\rm eff})$) on the Hertzsprung–Russell (H–R) diagram with the theoretical evolutionary tracks of Bertelli et al. (2008), which contains 912 models of AGB stars with a mass range of 0.55 to 2.50 $\mathrm{M}_\odot$. Fig. 2 compares the observationally derived position of our Mira target together with evolutionary tracks for a 1.2- $\mathrm{M}_\odot$ star taken from Bertelli et al. (2008). The figure suggests that the mass of W Hya is close to 1.6 $\mathrm{M}_\odot$ within an uncertainty of $\pm 0.36\,\mathrm{M}_\odot$ (which corresponds to a surface gravity of $\log g = -0.86 \pm 0.17$ and a metallicity of [Fe/H] = 0.78). The parameters that we deduced ourselves (i.e. $M_\star$, $\log g$ and [Fe/H] for W Hya) are labelled with an asterisk in Table B1 (Appendix B).

We selected stellar atmosphere models with parameters (detailed in the 'MARCS model' part of Table B1) as close as possible to those available from the spherical MARCS models. The chemical composition ('moderately CN-cycled' or 'heavily CN-cycled') are determined using the ^{12}CO/^{13}CO ratio. Note that although asymmetries in the CO line-forming region are clearly detected from $\phi_{\rm diff}$ of some stars (e.g. W Hya), we only use a spherical model as a first approximation.

[6] http://marcs.astro.uu.se.

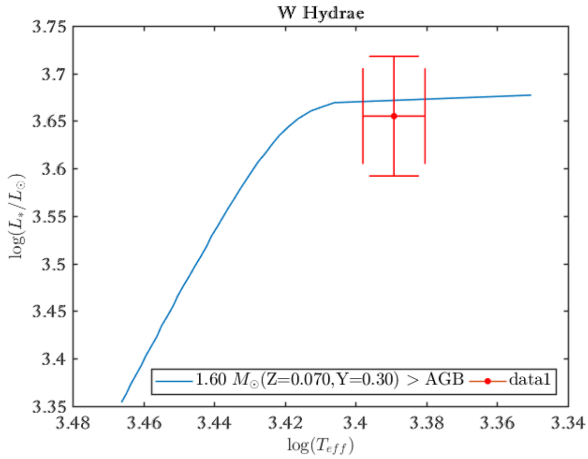

Figure 2. H–R diagram with the theoretical evolutionary track of the AGB for a 1.6-$\mathrm{M}_\odot$ star taken from Bertelli et al. (2008), with $Y = 0.30$ and $Z = 0.07$ (denoted by the blue solid line), and the observationally derived positions of the Mira star, W Hya (red filled circle with error bars).

To the CLV MARCS model of each star of our sample, we add a MOLsphere from a multilayer model, as described in detail in Section 4.2. Using temperature and pressure distributions of the downloaded MARCS model (Gustafsson et al. 2008) with the parameters cited in Table B1, we compute the corresponding monochromatic intensity profile and then the spectrum (as described in Ohnaka 2013), but this time using Turbospectrum software (Alvarez & Plez 1998; Plez 2012). In Section 4.2, we explain further how we use Turbospectrum and we introduce our new approach of multilayer MOLsphere modelling.

4.2 Multilayer MOLsphere model: PAMPERO

The first modelling of a star surrounded by a MOLsphere was done by Perrin et al. (2004) on the FLUOR/IOTA data of Betelgeuse (α Orionis) and Rasalgethi (α Herculis), as blackbodies, with five free parameters: the stellar angular diameter $\varnothing_\star$; the MOLsphere angular diameter (as one layer) $\varnothing_{\rm layer}$; the stellar temperature $T_\star = T_{\rm eff}$; the MOLsphere temperature $T_{\rm layer}$; optical depths τ_K, τ_L and $\tau_{11.15\,\mu\mathrm{m}}$ at the K, L and 11.15 μm bands, respectively. Ohnaka et al. (2009, 2011, 2012) and Ohnaka (2013) had a more sophisticated model, using MARCS models, for several different types of evolved stars using the VLTI/AMBER instrument at the K band, where the optical depth is deduced from the column density and temperature of specific molecules (e.g. CO) over one to two MOLsphere layers. Also, Montargès et al. (2014) mixed both approaches using the K-band VLTI/AMBER data of Betelgeuse for two molecules (CO and H_2O) but with the stellar atmosphere grids of ATLAS 9 (Castelli & Kurucz 2003; Kurucz 2005). The approach that we adopt in this paper is the same that of Ohnaka (2013), with stellar atmosphere grids of MARCS, using K-band VLTI/AMBER data, for the CO molecule, but with a continuous multilayer MOLsphere (with a path of $0.1R_\star$). Our aim is to study the temperature and molecular density distributions of the different MOLspheres of our sample.

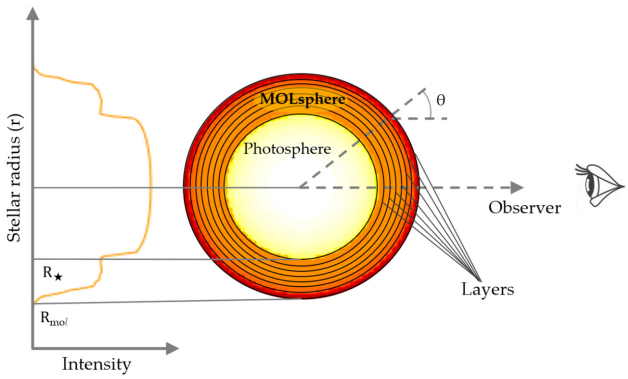

Figure 3. Schematic view of PAMPERO, where a continuous multilayer MOLsphere is surrounding a CLV MARCS model.

We have called our model/code PAMPERO. This code, which is written in MATLAB,[7] computes first the stellar CLVs using the preselected MARCS models (Table B1), by using Turbospectrum[8] (Alvarez & Plez 1998; Plez 2012) and its SPHLIMB algorithm, over the observed wavelength range taken from the listed CO lines of Goorvitch (1994).[9] These CLVs are computed through the Earth's atmospheric air. To correct the spectral splitting caused by the Earth's atmospheric air, we use the formula of Edlén (1966). For the attenuation correction, we deduced the average approximation from the attenuation factor formula for solar energy (Meinel & Meinel 1977) for polluted air at a zenith angle of 45°. The monochromatic visibilities are deduced using a simple Fourier transform of the monochromatic intensity profiles. Then, all the MARCS outputs (intensity profile, visibility and spectrum) were convolved with the AMBER spectral resolution ($\lambda/\Delta\lambda = 12\,000$). We adopt values of the modelled angular diameter that have optimum correspondence between the modelled and observed visibilities in the continuum for the three observational baselines. For our sample of evolved stars, although our AMBER data spatially resolve the MOLsphere in the individual CO lines and the modelled MARCS atmosphere alone predicts the spectra well, this is not sufficient to explain the observed behaviour of the visibilities. Indeed, the visibilities in the CO lines predicted by the MARCS model are too high, which means that either the extension of the real CO line-forming layer is much higher than the MARCS model prediction or there is an additional component contributing to the CO lines above the MARCS photosphere modelling. So, as can be seen, the theoretical spectra of strong molecular or atomic features, which are deduced only from the photospheric models, can be highly misleading. This was demonstrated, in the past, for BK Vir, α Boo and SW Vir by Ohnaka et al. (2012), Ohnaka & Morales Marín (2018) and Ohnaka et al. (2019), respectively, by using a MOLsphere model of two layers.

So, we need to add MOLspheres over our MARCS model CLVs to obtain visibilities which will be more consistent with the observations. Fig. 3 depicts a schematic view of our best model for SW Vir (see Section 5), at $\lambda = 2.2936\,\mu$m, with an angular diameter $\text{⌀}_\star$ and which is surrounded by a continuous multilayer MOLsphere. The analytical expression $I_{\star+\mathrm{mol}}(\text{⌀}_\star, \mu, \lambda, T_{\mathrm{mol}}, N_{\mathrm{mol}})$ of the CLV star and MOLsphere (where λ is the wavelength, T_{mol} is the temperature molecular distribution, N_{mol} is the column density molecular distribution, $\mu = \sqrt{1-(r/R_{mol})^2} = \cos\theta$ is related to the stellar radius r, which varies from 0 to the MOLsphere outer radius R_{mol} passing through the star radius $R_\star$, and θ is the angle between star centre direction and the line of sight), which we call simply I, is given as (e.g. Montargès et al. 2014):

$$I = \begin{cases} I_\star \exp(-\mu\tau_{\mathrm{mol}}) + I_{\mathrm{mol}}[1-\exp(-\mu\tau_{\mathrm{mol}})] & \text{if } \mu \le \mu_\star \\ I_{\mathrm{mol}}[1-\exp(-2\mu\tau_{\mathrm{mol}})] & \text{if } \mu > \mu_\star \end{cases}. \quad (1)$$

Here, $\mu_\star = \sqrt{1-(R_\star/R_{\mathrm{mol}})^2}$, τ_{mol} is the optical depth of the MOLsphere, I_{mol} denotes, according to (λ, T_{mol}), the Planck (blackbody) function of the MOLsphere, given by

$$I_{\mathrm{mol}} = \frac{2hc^2}{\lambda^5}\frac{1}{\exp(hc/\lambda K_{\mathrm{B}} T_{\mathrm{mol}}) - 1}, \quad (2)$$

where T_{mol} is the temperature of the MOLsphere, h is the Planck constant, c is the light velocity and K_{B} is the Boltzmann constant. $I_\star$ is the MARCS monochromatic stellar intensity according to (λ, μ), defined as (e.g. Ohnaka 2013):

$$I_\star = \int S_\lambda(\tau_\star)\exp(-\tau_\star)\,\mathrm{d}\tau_\star, \quad (3)$$

where S_λ is the source function and $\tau_\star$ is the stellar monochromatic optical depth at λ (for further details, see Gustafsson et al. 2008). For the MOLsphere, the monochromatic τ_{mol} is related to λ, the temperature and column density molecular distributions along the stellar radius $T_{\mathrm{mol}}(r/R_\star)$ and $N_{\mathrm{mol}}(r/R_\star)$ (which we define for more simplicity as T_{mol} and N_{mol}, respectively), and it is given by

$$\tau_{\mathrm{mol}} = \sum_{r/R_\star} N_{\mathrm{mol}}\sigma_{\mathrm{eff}}\frac{gf}{Q(T_{\mathrm{mol}})}\left[1-\exp\left(\frac{hc}{\lambda K_{\mathrm{SB}} T_{\mathrm{mol}}}\right)\right], \quad (4)$$

where K_{SB} is the Stefan–Boltzmann constant, σ_{eff} is the cross-section, $Q(T_{\mathrm{mol}})$ is the partition function specific for each molecule and the gf-value is the absorption oscillator strength (for further details, see Goorvitch 1994; Mangum & Shirley 2015).

If we can deduce the spectrum directly from I (equation 1) using the following simple and usual formula (e.g. Ohnaka 2013),

$$F = 2\pi\int_0^1 I(\mu)\mu d\mu, \quad (5)$$

then we have to derive the interferometric observables from the monochromatic intensity distribution of our target ($I_{\star+\mathrm{mol}}$; equation 1) using the Van Cittert–Zernike theorem (van Cittert 1934; Zernike 1938). Because of the spherical symmetry specificity of cool evolved stars, it is more practical to derive the visibility $V(B, \lambda)$ using the Hankel transform and utilizing the assumed $\text{⌀}_\star$ of the studied object for each projected baseline B at λ, as follows (e.g. Montargès et al. 2014):

$$V = \frac{2\pi\int_0^{R_{\mathrm{mol}}} I\,J_0(\pi B\text{⌀}_\star r/\lambda)r\,\mathrm{d}r}{F}. \quad (6)$$

Here, I is the CLV of a star surrounded by the MOLsphere as defined in equation (1), J_0 is the zeroth-order Bessel function of the first kind and r is the radius along the star and its MOLsphere (see Fig. 3).

So, from the visibility (equation 6; $V = |V|\,\mathrm{e}^{-\mathrm{i}\phi_{\mathrm{diff}}}$), we deduce the differential phase $\phi_{\mathrm{diff}}(\lambda, B)$ and the closure phase $\Psi(\lambda) = \sum_B \phi_{\mathrm{diff}}(\lambda, B)$. As explained previously, our model is spherically symmetric, which means that all the ϕ_{diff} on the first visibility lobe are zero, whereas the ϕ_{diff} sign is flipped in the second visibility lobe with a π value. Finally, for a more rigorous comparison between the model and the observations, we interpolate our modelled spectro-interferometric data (F, V, ϕ_{diff}, Ψ) at observed wavelengths (λ_{obs}),

[7] MATrix LABoratory.
[8] Available at http://www.pages-perso-bertrand-plez.univ-montp2.fr/.
[9] Available with a large list of other molecules at https://nextcloud.lupm.univ-montp2.fr/s/r8pXijD39YLzw5T.

Table 3. Summary of the maximum size of the photospheric MARCS model, Max($R_{\rm MARCS}$) as a function of $r/R_\star$, for each studied star of our sample.

Star	Max($R_{\rm MARCS}$)
BK Vir	$1.1581R_\star$
α Boo	$1.0207R_\star$
SW Vir	$1.1581R_\star$
γ Cru	$1.0358R_\star$
λ Vel	$1.0159R_\star$
α Sco	$1.0541R_\star$
W Hya	$1.1099R_\star$

which were converted to the laboratory frame previously (as explained in Section 2).

Regarding the temperature and density distributions along the stellar radius ($r/R_\star$), which are the molecular column density (in this paper, we focus only on the carbon monoxide molecule $N_{\rm mol} = N_{\rm CO}$) and the MOLsphere's temperature $T_{\rm mol}$ of $I_{\star+{\rm mol}}(\mu, \lambda, T_{\rm mol}, N_{\rm mol})$ of equation (1), we assume that they are inversely proportional to $(r/R_\star)^\zeta$, as follows:

$$T_{\rm mol} = T_0 \left[\left(\frac{r}{R_{\rm mol,0}} \right)^{-\zeta_{\rm T}} \right];$$
$$N_{\rm mol} = N_0 \left[\left(\frac{r}{R_{\rm mol,0}} \right)^{-\zeta_{\rm N}} \right]. \quad (7)$$

Here, $\zeta_{\rm T}$ and $\zeta_{\rm N}$ are coefficients, T_0 and N_0 are the temperature and the column density of the first MOLsphere layer, respectively, and $r/R_{\rm mol,0}$ is derived from the normalization $(r/R_\star)/(R_{\rm mol,0}/R_\star)$, where $R_{\rm mol,0}$ is the inner radius of the first MOLspheric layer.

Whatever the number of MOLsphere layers, by fixing the thickness (e.g. $0.1R_\star$), our numerical model needs only six free parameters (i.e. T_0, N_0, $\zeta_{\rm T}$, $\zeta_{\rm N}$, $R_{\rm mol,0}$ and $R_{\rm mol,end}$), where $R_{\rm mol,0}$ and $R_{\rm mol,end}$ are the upper and lower radius boundaries of our MOLsphere. We also adjust two other parameters: the angular diameter $\oslash_\star$, in order to settle modelled visibilities at the same level as those observed at the continuum, and the MOLspheric microturbulent velocity ($v_{\rm micro,mol}$), which affects only the width of the molecular lines. In general, we find $v_{\rm micro,mol}$ values in the literature. Otherwise, we got the best model with the six free parameters listed above. We adjust $\oslash_\star$ within its bounds of uncertainty and we play with $v_{\rm micro,mol}$ until we get the best match, in terms of the width of the molecular lines, with observations (with the minimum value of χ^2).

To avoid an overlap with the MARCS photospheric model, which is extended up to 1 $R_\star$ for our sample of stars, the radius of the first/inner layers of all our MOLsphere models is set to be equal to, or larger than, the maximum size of the photospheric MARCS model of each studied star. Table 3 summarizes the maximum size of all MARCS photospheric models of our targets, star by star.

Fig. 4 describes intensity maps and CLVs of our code PAMPERO, according to the normalized flux, for the best model for SW Vir (see Section 5), at five different wavelengths; at the continuum ($\lambda = 2.2926\,\mu$m), around the CO band head ($\lambda = 2.2936$, 2.2938 and 2.2943 μm) and on one individual CO line ($\lambda = 2.2973\,\mu$m).

In Section 5, and by combining a χ^2 minimization method and a fine grid approach, we summarize, according to the observations, the best modelled molecular behaviour that we found with PAMPERO ($T_{\rm mol}$ and $N_{\rm co}$), target by target.

5 RESULTS AND DISCUSSION

We present the best PAMPERO models that were found for the entire sample of targets. Indeed, by using a new atmospheric temperature–density distribution approach, we were able to resolve the extended MOLspheres for several kinds of evolved stars, including normal K–M giants, Mira stars and red giants, in the IR (K band) for CO, as shown in Figs D1–D8. For practical reasons, all the results of this section are summarized in Table B1 and the corresponding figures are shown in Appendix D. The uncertainties calculated by our χ^2 minimization method are described in Hadjara et al. (2014, see section 4).

We present our results as follows. We follow the chronological order of observations, and maintain the same colour code as defined in Section 2 and presented in Fig. 1. For the best model of each star, we show first the MOLsphere's CO column density $N_{\rm CO}$ and temperature $T_{\rm mol}$ along the stellar radius ($r/R_\star$). Next, we present the spectro-interferometric data – the normalized flux ($F/F_{\rm Continuum}$), the visibilities (V) corresponding to their respective baselines (B) and the closure phase Ψ, all according to the wavelength (λ) – overplotted with the results of our best model (continuous black line). In the same figure, we show in the title, next to the name of the star, the reduced χ^2-value (hereafter simply χ^2). By applying our new continuous and multilayer MOLsphere approach, we present in this section the published results of three stars, BK Vir, α Boo and SW Vir (where we compare, for these stars, the results of our multilayer approach with the results from the bi-layer approach, using the values given in Table B1 and computations with PAMPERO). Then, we present the new results of four evolved stars (including one Mira star observed for two epochs): γ Cru, λ Vel, α Sco and W Hya (Fig. D1–D8). We determine the uncertainties of the six free parameters (i.e. T_0, N_0, $\zeta_{\rm T}$, $\zeta_{\rm N}$, $R_{\rm mol,0}$ and $R_{\rm mol,end}$) that we presented in Section 4.2, using the same method that was used for the other model, which is dedicated to hot active stars (SCIROCCO; Hadjara et al. 2014, 2018; Hadjara 2015), when the χ^2-minimization was used, after localizing the global minimums by using a large grid of six free parameters. The results are given in Table C1 in Appendix C. For α Sco, we improved the fitting with an ad hoc manipulation; by manually adjusting the values $T_{\rm mol}$ and $N_{\rm co}$ for a few layers, and using a priori values that we determined from the MOLspheric model for this star. We assume that α Sco has a MOLsphere with a convective behaviour (Ohnaka, Weigelt & Hofmann 2017a).

5.1 BK Vir

The best PAMPERO model fit for BK Vir found a total thickness of $3.3R_\star$ containing 33 layers, each with a thickness of $0.1R_\star$. We found a temperature–density distribution of $T_{\rm mol}(r/R_\star)$ and $N_{\rm CO}(r/R_\star)$, according to equation (7), with a MOLspheric temperature of the first layer of $T_0 = 2010$ K with a coefficient of $\zeta_{\rm T} = 0.35$, and a MOLspheric CO column density of the first layer at $N_0 = 10^{22.3}$ mol cm^{-2} with a coefficient of $\zeta_{\rm N} = 18$. The first two plots in Fig. D1 depict the temperature–density distribution $T_{\rm mol}(r/R_\star)$ and $N_{\rm CO}(r/R_\star)$, respectively, where both distributions start from $R_{\rm mol,0} = 1.2R_\star$ and decrease to $R_{\rm mol,end} = 4.5R_\star$ with the coefficients of $\zeta_{\rm T}$ and $\zeta_{\rm N}$, respectively. The MOLspheric temperature–density distribution shows a decrease in temperature and $N_{\rm CO}$ from $T_{\rm mol}(R_{\rm mol,0}/R_\star) = 2010$ K to $T_{\rm mol}(R_{\rm mol,end}/R_\star) = 1266$ K and $N_{\rm CO}(R_{\rm mol,0}/R_\star) = 10^{22.3}$ to $N_{\rm CO}(R_{\rm mol,end}/R_\star) = 10^{12}$ mol cm^{-2}, respectively. We adjusted $\oslash_\star = 10.6$ mas to obtain the best fit between the model and the observed visibilities in the continuum. According to Ohnaka et al. (2012, and references therein), we fixed $v_{\rm micro,mol} = v_{\rm micro} =$

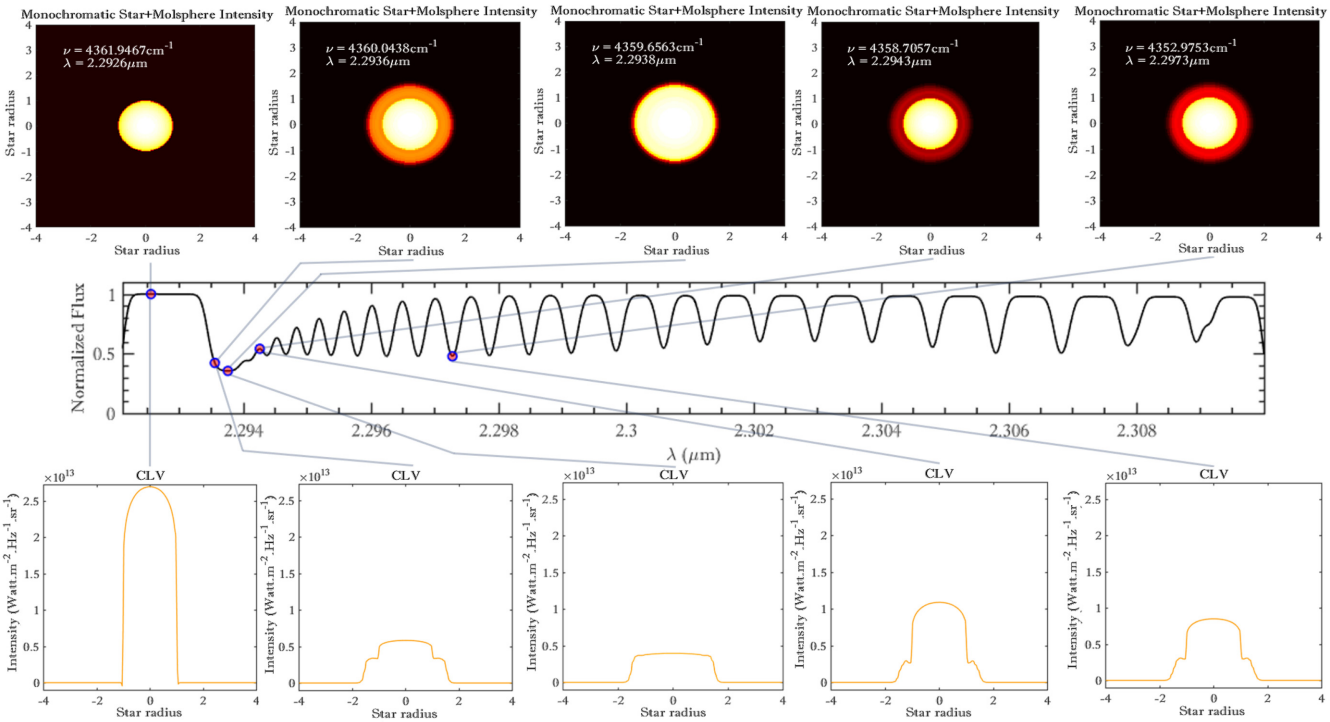

Figure 4. PAMPERO intensity maps and CLVs, according the normalized flux, for the best model for SW Vir, at the continuum ($\lambda = 2.2926$ μm), around the CO band head ($\lambda = 2.2936$, 2.2938 and 2.2943 μm) and on one individual CO line ($\lambda = 2.2973$ μm).

4 km s^{-1} in order to obtain the best agreement between the width of modelled molecular lines and the observations. The bottom portion of Fig. D1 shows a comparison between the modelled and observed normalized flux $F/F_{\rm Continuum}(\lambda)$, visibilities $V(\lambda)$ and closure phases.

By examining the visibility plots, we observe slight differences in the variations of the modelled data with respect to observations at the continuum (Fig. D1), which means that the target is not perfectly spherical. Miguel (2014) demonstrated that a hotspot(s) or dark spot(s) could affect visibility. We interpret the discrepancy in the fit of the CO band head for the second visibility ($B = 31.82$ m) due to the presence of a hotspot(s) or a dark spot(s) on the edge of the MOLsphere (around $4.4R_\star$), which only appears around $\lambda = 2.294$ μm (see Fig. 4). We cannot determine the position or the number of spots with our sparse (u, v) coverage (Fig. 1). Alternatively, the discrepancy between the model and observed spectrum at $\lambda = 2.299$ and 2.305 μm is due to the residuals of the strong telluric lines, which appear in all the observed spectra of all targets.

At first glance, the best continuous multilayer MOLsphere model (PAMPERO) for BK Vir agrees with that of the discontinuous two-layer model presented by Ohnaka et al. (2012), especially at the first layer, where Ohnaka et al. (2012) found 1.2–1.25$R_\star$ ($T_0 = 1900$–2100 K, $N_0 = 1$–2×10^{22} mol cm^{-2}), while our results show 1.18–1.22$R_\star$ ($T_0 = 1960$–2060 K, $N_0 = 1.6$–2.5×10^{22} mol cm^{-2}). However, we find noticeable disagreement for the second layer, especially for $N_{\rm CO}$ where Ohnaka et al. (2012) found 2.5–3$R_\star$ ($T = 1500$–2100 K, $N = 10^{19}$–10^{20} mol cm^{-2}) and our results indicate ($T = 1400$–1600 K, $N = 10^{15}$–10^{17} mol cm^{-2}), for the same size. We attribute this large difference in density to the fact that the discontinuous two-layer model does not take into account the effect of a continuous MOLsphere, which may overestimate the temperature–density parameters of a large MOLsphere area when using a single thin layer.

Note that we also checked the results of BK Vir by another uniform-disc value of its calibrator β Crv (3.40 ± 0.30 mas; Richichi & Percheron 2005) instead of JSDC (3.27 ± 0.36 mas; Bourges et al. 2017). There is no significant difference between these two results, except the adjusted $\varnothing_\star$ of BK Vir, which is 10.75 mas instead of 10.6 mas.

5.2 α Boo

For α Boo, the best PAMPERO model fit shows a total thickness of 0.5$R_\star$ for five layers, each with a thickness of 0.1$R_\star$. The temperature–density distribution is $T_0 = 1650$ K with a coefficient of $\zeta_{\rm T} = 6.56$, and $N_0 = 10^{19.2}$ mol cm^{-2} with a coefficient of $\zeta_{\rm N} = 30$. The first two plots in Fig. D2 depict $T_{\rm mol}(r/R_\star)$ and $N_{\rm CO}(r/R_\star)$, where both distributions start from $R_{\rm mol,0} = 2.5R_\star$ and decrease to $R_{\rm mol,end} = 3R_\star$ with the coefficients of $\zeta_{\rm N}$ and $\zeta_{\rm T}$, respectively.

The MOLspheric temperature–density distribution shows a decrease in temperature and $N_{\rm CO}$ from $T_{\rm mol}(R_{\rm mol,0}/R_\star) = 1650$ K to $T_{\rm mol}(R_{\rm mol,end}/R_\star) = 499$ K and $N_{\rm CO}(R_{\rm mol,0}/R_\star) = 10^{19.2}$ mol cm^{-2} to $N_{\rm CO}(R_{\rm mol,end}/R_\star) = 10^{16.8}$ mol cm^{-2}, respectively. We adjusted $\varnothing_\star = 20.7$ mas to obtain the best fit between the model and the observed visibilities in the continuum, whilst we fixed $v_{\rm micro,mol} = v_{\rm micro} = 2$ km s^{-1} (as discussed by Ohnaka 2014, and references therein), in order to obtain the best agreement between the width of modelled molecular lines and the observations. The bottom portion of Fig. D2 shows a comparison between modelled and observed normalized flux $F/F_{\rm Continuum}(\lambda)$, visibilities $V(\lambda)$ and closure phases.

We observe slight differences for visibilities in the variations of modelled data with respect to observations at the continuum (Fig. D2), which means that the target is not perfectly spherical. For the third visibility, at the third baseline ($B = 21.83$ m), our fit has a lower goodness of fit with respect to the first visibilities ($B = 7.27$ m and $B = 14.56$ m) but it remains inside the 1σ uncertainty, which is acceptable.

By assuming a continuity of the MOLsphere, we are adding another scenario to the case of α Boo's MOLsphere. While Ohnaka & Morales Marín (2018) propose two different MOLspheric layers, where the inner layer is close to the photosphere at $1.04 \pm 0.02R_\star$ with $T_{\rm mol} = 1600 \pm 400$ K and $N_{\rm CO} = 10^{20\pm0.3}$ mol cm^{-2}, and the outer layer is at $2.6 \pm 0.2R_\star$ with $T_{\rm mol} = 1800 \pm 100$ K and $N_{\rm CO} = 10^{19\pm0.15}$ mol cm^{-2}, we suggest the possibility of continuous distribution. Indeed, Ayres, Brown & Harper (2003) argue that RGB stars host a cool CO area (which they called COMosphere $\sim$1000 K) between the photosphere and the chromosphere, which is crossed by an important stellar wind because of the intense magnetic field of this type of star (Alfvén-wave-driven wind; e.g. Suzuki 2007; Airapetian, Carpenter & Ofman 2010). Our best PAMPERO model proposes a continuous distribution with a $T_{\rm mol}$ value close to that of the inner layer given by Ohnaka & Morales Marín (2018) and an $N_{\rm co}$ value close to the outer value given by Ohnaka & Morales Marín (2018), with a lower temperature of $\sim$1300 K at $2.6R_\star$. The magnetic field loops combined with the stellar wind, which expels the photospheric matter over long distances where we suspect that the COMosphere may overlap the chromosphere (which remains a topic of debate), could explain the heating mechanism that is present in the outer atmosphere. Maybe Arcturus has a discontinued MOLspheric distribution as suggested by Ohnaka & Morales Marín (2018), but our model demonstrates that the only continuous MOLspheric distribution that is possible is that from $2.5 \pm 0.2R_\star$, where we checked every conceivable scenario of continuous MOLspheric distributions.

5.3 SW Vir

Our best PAMPERO model fit for SW Vir shows a total thickness of $1.8R_\star$ for 18 layers, each with a thickness of $0.1R_\star$. The temperature–density distribution of $T_{\rm mol}(r/R_\star)$ and $N_{\rm CO}(r/R_\star)$, according to equation (7), has a MOLspheric first-layer temperature of $T_0 = 1950$ K with a coefficient of $\zeta_{\rm T} = 0.06$, and a MOLspheric CO column density $N_0 = 10^{22.5}$ mol cm^{-2} with a coefficient of $\zeta_{\rm N} = 30$. The first two plots in Fig. D3 depict the temperature–density distribution of $T_{\rm mol}(r/R_\star)$ and $N_{\rm CO}(r/R_\star)$, respectively, where both distributions start from $R_{\rm mol,0} = 1.2R_\star$ and decrease to $R_{\rm mol,end} = 3R_\star$ with the coefficients of $\zeta_{\rm T}$ and $\zeta_{\rm N}$, respectively. The MOLspheric temperature–density distribution shows a decrease in temperature and $N_{\rm CO}$ from $T_{\rm mol}(R_{\rm mol,0}/R_\star) = 1950$ K to $T_{\rm mol}(R_{\rm mol,end}/R_\star) = 1846$ K and from $N_{\rm CO}(R_{\rm mol,0}/R_\star) = 10^{22.5}$ to $N_{\rm CO}(R_{\rm mol,end}/R_\star) = 10^{10.6}$, respectively. We adjusted $\oslash_\star = 16.7$ mas to obtain the best fit between the model and the observed visibilities in the continuum. According to Ohnaka et al. (2019, and references therein), we fixed $v_{\rm micro,mol} = v_{\rm micro} = 3.6$ km s^{-1} in order to obtain the best agreement between the width of modelled molecular lines and the observations. The bottom portion of Fig. D3 shows a comparison between the modelled and observed normalized flux $F/F_{\rm Continuum}(\lambda)$, visibilities $V(\lambda)$ and closure phases.

From the visibilities, we can observe that our modelled data are of approximately the same amplitudes with respect to the observations at the continuum (Fig. D3), which corresponds to a quasi-perfectly spherical target. As for BK Vir, we interpret the discrepancy in the fit on the CO band head (and some other individual lines) of the second visibility ($B = 19.64$ m) due to the presence of a hotspot(s) or a dark spot(s) on the MOLsphere and we cannot determine the position or the number with our sparse (u, v) coverage (as demonstrated by Miguel 2014).

As for BK Vir, at first glance, our best continuous multilayer MOLsphere model (PAMPERO) for SW Vir agrees within their 1σ uncertainties with that of the discontinuous two-layer solution given by Ohnaka et al. (2019), particularly at the first layer, where Ohnaka et al. (2019) found $1.3 \pm 0.1R_\star$ ($T_0 = 2000 \pm 100$ K, $N_0 = 1 - 3 \times 10^{22}$ mol cm^{-2}) while our results show at the same size ($T_0 = 1940 \pm 60$ K, $N_0 = 10^{22.5} - 10^{20.5}$ mol cm^{-2}). However, we find noticeable disagreement for the second layer, especially for $N_{\rm CO}$ where Ohnaka et al. (2019) found $2.0 \pm 0.2R_\star$ ($T = 1700 \pm 100$ K, $N = 2 \times 10^{19} - 2 \times 10^{20}$ mol cm^{-2}) while our results indicate at the same size ($T = 1880 - 1903K$, $N = 10^{14.6} - 10^{17.22}$ mol cm^{-2}). We attribute this large difference in density, for BK Vir, to the fact that the discontinuous two-layer model does not take into account the effect of a continuous MOLsphere, which may overestimate the temperature–density parameters of a large MOLsphere area when using a single thin layer.

Axial symmetry is not usual for normal K–M giant stars. We observe axisymmetrical CSEs, in general, on post-AGB stars and planetary nebulae (Dijkstra & Speck 2006), whereas most AGB stars show spherically symmetric envelopes (especially O-rich stars; Cruzalèbes et al. 2015). As a result of a *Hipparcos* radial velocity study of a sample of M giants, Famaey et al. (2009) suspected that SW Vir could be a binary system. Niyogi, Speck & Volk (2011) used Gemini/MICHELLE IR data of SW Vir and deduced, from the spectra, an axisymmetric dust shell that cannot be attributed to a simple radial temperature variation. Hence, they strongly favour the influence of a companion. Unfortunately, because of the array configuration of our sparse (u, v) coverage (see Fig. 1), it is impossible for us to deduce, by projection, the corresponding declination and right ascension photocentre displacements. Therefore, we are unable to confirm the existence of any axial symmetry of the CSE of SW Vir, as observed by Niyogi et al. (2011).

5.4 γ Cru

The best PAMPERO model fit for γ Cru found a total thickness of $0.1R_\star$ containing a single layer. We found a temperature–density distribution of $T_0 = 960$ K with a coefficient of $\zeta_{\rm T} = 0.1$, and $N_0 = 10^{21.5}$ mol cm^{-2} with a coefficient of $\zeta_{\rm N} = 50$. The first two plots in Fig. D4 depict the temperature–density distribution $T_{\rm mol}(r/R_\star)$ and $N_{\rm CO}(r/R_\star)$, where both distributions start from $R_{\rm mol,0} = 5.15R_\star$ and slightly decrease until $R_{\rm mol,end} = 5.25R_\star$ with the coefficients of $\zeta_{\rm T}$ and $\zeta_{\rm N}$, respectively.

The MOLspheric temperature–density distribution shows a slight decrease in temperature and $N_{\rm CO}$ from $T_{\rm mol}(R_{\rm mol,0}/R_\star) = 960$ K to $T_{\rm mol}(R_{\rm mol,end}/R_\star) = 958$ K and from $N_{\rm CO}(R_{\rm mol,0}/R_\star) = 10^{21.5}$ mol cm^{-2} to $N_{\rm CO}(R_{\rm mol,end}/R_\star) = 10^{21.1}$ mol cm^{-2}, respectively. We adjusted $\oslash_\star = 24.7 \pm 0.4$ mas to obtain the best fit between the model and the visibilities in the continuum. According to Ohnaka (2014, and references therein) we fixed $v_{\rm micro,mol} = v_{\rm micro} = 2$ km s^{-1} in order to obtain the best agreement between the width of modelled molecular lines and the observations. The bottom portion of Fig. D4 shows a comparison between the modelled and observed normalized flux $F/F_{\rm Continuum}(\lambda)$, visibilities $V(\lambda)$ and closure phases.

The modelled visibilities are of approximately the same amplitudes with respect to the observations at the continuum (Fig. D4),

only by adjusting the angular size ($\varnothing_\star = 24.7 \pm 0.4$ mas), which shows that the target is not perfectly spherical.

γ Cru is an RGB star (like α Boo), and hence should host a MOLsphere/COMosphere (of $T_{\rm mol} \sim 1000$ K; Ayres et al. 2003). Instead, it presents a solution of a thin CO layer, located far from the photosphere, because it is pushed by an important stellar Alfvén-wave-driven wind (Suzuki 2007; Airapetian et al. 2010).

5.5 λ Vel

For λ Vel, the best PAMPERO fit model shows a total thickness of $0.5R_\star$ for five layers, each with a thickness of $0.1R_\star$. The temperature–density distribution is $T_0 = 1000$ K with a coefficient of $\zeta_{\rm T} = 0.1$, and $N_0 = 10^{21.5}$ mol cm^{-2} with a coefficient of $\zeta_{\rm N} = 50$. The first two plots in Fig. D5 depict the temperature–density distribution $T_{\rm mol}(r/R_\star)$ and $N_{\rm CO}(r/R_\star)$, where both distributions start from $R_{\rm mol,0} = 4.5R_\star$ to decrease to $R_{\rm mol,end} = 5.0R_\star$ with the coefficients of $\zeta_{\rm T}$ and $\zeta_{\rm N}$, respectively.

The MOLspheric temperature–density distribution shows a decrease in temperature and $N_{\rm CO}$ from $T_{\rm mol}(R_{\rm mol,0}/R_\star) = 1000$ K to $T_{\rm mol}(R_{\rm mol,end}/R_\star) = 990$ K and from $N_{\rm CO}(R_{\rm mol,0}/R_\star) = 10^{21.5}$ mol cm^{-2} to $N_{\rm CO}(R_{\rm mol,end}/R_\star) = 10^{19.2}$ mol cm^{-2} respectively. We adjusted $\varnothing_\star = 11.3$ mas to obtain the best fit between the model and the observed visibilities in the continuum, and we fixed $v_{\rm micro,mol} = v_{\rm micro} = 2$ km s^{-1} in order to obtain the best agreement between the width of modelled molecular lines and the observations. The bottom portion of Fig. D5 shows a comparison between the modelled and observed normalized flux $F/F_{\rm Continuum}(\lambda)$, visibilities $V(\lambda)$ and closure phases.

The modelled visibilities are approximately the same in amplitudes with respect to the observations at the continuum (slightly less at the biggest baseline $B = 27.76$ m; see Fig. D5), which means that the symmetry of our target is not perfectly spherical but better than for γ Cru. We interpret the bad fit on the CO band head on the visibilities as the presence of a hotspot(s) or a dark spot(s) on the MOLsphere for which we cannot determine either the position or the number with our sparse (u, v) coverage (as demonstrated by Miguel 2014).

λ Vel should be more an RGB star than an AGB star (Kiss & Bedding 2003), just as α Boo and γ Cru, and we expect a MOLsphere/COMosphere (of $T_{\rm mol} \sim 1000$ K; Ayres et al. 2003). Instead, it presents a solution with a thick CO layer, which is far from the photosphere, because of an important stellar Alfvén-wave-driven wind (Suzuki 2007; Airapetian et al. 2010).

5.6 α Sco

Our best PAMPERO fit model for α Sco shows a total thickness of $0.7R_\star$ for seven layers, each with a thickness of $0.1R_\star$. The temperature–density distribution is of $T_0 = 2350$ K with a coefficient of $\zeta_{\rm T} = 1$, and $N_0 = 10^{21.5}$ mol cm^{-2} with a coefficient of $\zeta_{\rm N} = 35$. The first two plots in Fig. D6 depict the temperature–density distribution $T_{\rm mol}(r/R_\star)$ and $N_{\rm CO}(r/R_\star)$, where both distributions start from $R_{\rm mol,0} = 1.06R_\star$ to decrease to $R_{\rm mol,end} = 1.76R_\star$ with the coefficients of $\zeta_{\rm T}$ and $\zeta_{\rm N}$, respectively. The MOLspheric temperature–density distribution varies from $T_{\rm mol}(R_{\rm mol,0}/R_\star) = 2350$ K to $T_{\rm mol}(R_{\rm mol,end}/R_\star) = 1900$ K with a stochastic distribution along $r/R_\star$ (with two peaks $T_{\rm mol}(1.36R_\star) = 3600$ K and $T_{\rm mol}(1.66R_\star) = 2200$ K and two floods $T_{\rm mol}(1.16R_\star) = 1850$ K and $T_{\rm mol}(1.56R_\star) = 2000$ K, alternatively) and from $N_{\rm CO}(R_{\rm mol,0}/R_\star) = 10^{21.5}$ mol cm^{-2} to $N_{\rm CO}(R_{\rm mol,end}/R_\star) = 10^{19.2}$ mol cm^{-2} (with a flood of $N_{\rm CO}(1.46R_\star) = 10^{16.63}$ mol cm^{-2}), respectively. Without this ad hoc manipulation for $T_{\rm mol}$ and $N_{\rm co}$ of a few layers, the first modelled visibility is high with respect to the observation.

We adjusted $\varnothing_\star = 37$ mas to obtain the best fit between the model and the observed visibilities in the continuum. According to Ohnaka (2014, and references therein), we fixed $v_{\rm micro,mol} = v_{\rm micro} = 5$ km s^{-1} in order to obtain the best agreement between the width of modelled molecular lines and the observations. The bottom portion of Fig. D6 shows a comparison between the modelled and observed normalized flux $F/F_{\rm Continuum}(\lambda)$, visibilities $V(\lambda)$ and closure phases.

The modelled visibilities are of approximately the same amplitudes with respect to the observations at the continuum (Fig. D6), which means that the target is quasi-spherical, as demonstrated by the recent velocity-resolved images of Antares (Ohnaka et al. 2017a).

α Sco is an RSG, and its photosphere hosts large granules (instead of 2–10 million present on the Sun, as predicted by Schwarzschild 1975). These granules were suspected to be caused principally by a convection phenomenon (Haubois et al. 2009; Ohnaka et al. 2009, 2011; Chiavassa et al. 2010, 2011; Montargès et al. 2014), but Ohnaka et al. (2017a) deduced that this phenomenon of upwelling and down-drafting motions cannot by itself explain the atmospheric extension and turbulent motions observed on Antares. Indeed, Ohnaka et al. (2017a) deduced by its images a MOLsphere size of $R_{\rm mol} \sim 1.7R_\star$ with velocities of $V_{\rm mol} \sim -10$ to $+20$ km s^{-1}, indicating that the observed atmospheric extension and its density are much larger than theoretically predicted by Arroyo-Torres et al. (2015). Our Antares results (Fig. D6 and Table B1) confirm the recent MOLspheric CO size $R_{\rm mol} \sim 1.7R_\star$ of Ohnaka et al. (2017a) and its stochastic behaviour, with upwelling and down-drafting motions, as we can deduce from our temperature–density distributions. Therefore, we suggest a convective MOLsphere, just after the stellar convective area and its granules (in a continuous manner along the stellar radii) to interpret our results. Indeed, only a MOLsphere with a convective behaviour could explain this kind of temperature–density distribution $T_{\rm mol}(r/R_\star)$ and $N_{\rm CO}(r/R_\star)$. To confirm our findings, further work is needed using theoretical models of RSGs (e.g. three-dimensional convective models; Chiavassa et al. 2011; Arroyo-Torres et al. 2015). We have to keep in mind that our solution is a rough estimation of the MOLsphere of α Sco, because it is very difficult to model the stochasity of the temperature–density distribution. What we present here is only the mean values of $T_{\rm mol}(r/R_\star)$ and $N_{\rm CO}(r/R_\star)$. In addition, we interpret the poorer fit on the CO band head of the second and third visibilities due to the presence of a hotspot(s) or a dark spot(s) on the MOLsphere. We are unable to determine the position and number of spots with our sparse (u, v) coverage (as demonstrated by Miguel 2014).

5.7 W Hya

W Hya is a Mira star with magnitude variability $\Delta V = 7.7$–11.6 for a cyclic period of 361 d (GCVS version 5.1; Samus' et al. 2017). We study the H–R K-band AMBER data of this star at two luminosity phases: post-minimum light (phase 0.59) and pre-maximum light (phase 0.77).

The best-fitting PAMPERO models for W Hya (phases 0.59 and 0.77) found a total thickness of $0.4R_\star$ containing four layers, each with a thickness of $0.1R_\star$. We found temperature–density distributions of $T_0 = 1950$ K with a coefficient of $\zeta_{\rm T} = 0.6$, and $N_0 = 10^{22.7}$ mol cm^{-2} with a coefficient of $\zeta_{\rm N} = 10$ at post-

minimum light, and $T_0 = 2000$ K with a coefficient of $\zeta_T = 0.6$, and $N_0 = 10^{22.7}$ mol cm^{-2} with a coefficient of $\zeta_N = 10$ at the pre-maximum. The first two plots in Figs D7 and D8 depict the temperature–density distribution $T_{mol}(r/R_\star)$ and $N_{CO}(r/R_\star)$, which starts from $R_{mol,0} = 1.3R_\star$ and decreases to $R_{mol,end} = 1.7R_\star$ for the post-minimum phase. For the pre-maximum phase, the temperature–density distribution $T_{mol}(r/R_\star)$ and $N_{CO}(r/R_\star)$ starts from $R_{mol,0} = 1.4R_\star$ and decreases to $R_{mol,\ end} = 1.8R_\star$, both with coefficients of ζ_T and ζ_N, respectively.

The MOLspheric thermal distribution of the phase 0.59 decreases from $T_{mol}(R_{mol,0}/R_\star) = 1950$ K to $T_{mol}(R_{mol,end}/R_\star) = 1660$ K, while the phase 0.77 decreases from $T_{mol}(R_{mol,0}/R_\star) = 2000$ K to $T_{mol}(R_{mol,end}/R_\star) = 1720$ K, when the MOLspheric CO density distributions of both luminosity phases decrease from $N_{CO}(R_{mol,0}/R_\star) = 10^{22.7}$ mol cm^{-2} to $N_{CO}(R_{mol,end}/R_\star) = 10^{21.6}$ mol cm^{-2}.

Our best-fitting models for these two luminosity phases show a clumpy MOLsphere with a total thickness ∼10 per cent greater at post-minimum light ($\oslash_\star = 43.75 \pm 0.75$ mas, $R_{mol,end} = 1.7R_\star$) than at the pre-maximum light ($\oslash_\star = 39$ mas, $R_{mol,end} = 1.8R_\star$). The MOLspheric temperature of the first layer is slightly higher at the pre-maximum ($T_0 = 2000$ K) than at the post-minimum ($T_0 = 1950$ K), with almost the same T_0 taking into account the uncertainty of ±50 K for both, while the CO column density and MOLspheric temperature coefficients appear to stay the same ($N_0 = 10^{22.7}$ mol cm^{-2}, $\zeta_N = 10$ and $\zeta_T = 0.6$). However, the thermal distribution seems to be higher at the phase 0.77 than at the phase 0.59, while the CO density distribution appears to stay the same. The width of modelled CO lines agrees with the observations, with a microturbulent velocity of $v_{micro,mol} = 3.7$ km s^{-1} for the phase 0.59, while for the phase 0.77, the value of 4 km s^{-1} seems to be the optimum $v_{micro,\ mol}$. This means that the star's activity also affects the microturbulent velocity, implying that the activity and microturbulent velocity are proportional to each other.

We perturbed $\oslash_\star = 43.75$ mas by ±0.75 mas at the post-minimum, to obtain a good fit between the amplitudes of the three modelled visibilities compared with the observed visibility, where we fixed $\oslash_\star = 39$ mas at the pre-maximum. This implies that W Hya seems to be more spherical at phase 0.59 than at phase 0.77. We interpret this as the light emitted by W Hya at the maximal activity disrupting the symmetry of the MOLsphere material obtained during the minimal activity due to the gravitational force. We observe, among our sample of evolved stars, that W Hya has the highest column density with $N_{CO} = 10^{22.7}$ mol cm^{-2} and the lowest coefficient $\zeta_N = 10$. We explain this behaviour by the fact that W Hya is a Mira variable star with a regular cyclic activity, which feeds the interstellar medium continuously (every 361 d).

We interpret the poor fit on the CO band head (and some other individual lines) with the same visibilities (on the both phases) due to the presence of a hotspot(s) or a dark spot(s) on the MOLsphere. We cannot determine the position or the number of spots with our sparse (u, v) coverage (as demonstrated by Miguel 2014).

Our average MOLspheric temperature and CO MOLspheric sizes of W Hya agree well with the results of a prior study, which found $T_{mol} \sim 1500$ K and $R_{mol} = 1.9$–$3.0R_\star$ (Ohnaka et al. 2016).

6 CONCLUSIONS

Using the differential interferometry technique of VLTI/AMBER, we were able to spatially resolve the individual CO first overtone lines of a sample of different evolved stars – the RSG α Sco, the RGB stars α Boo and γ Cru, the K giant λ Vel, the normal M giants BK Vir and SW Vir, and the Mira variable star W Hya – at two different luminosity phases. The uniform-disc diameters in the CO lines are distinctly higher compared with the continuum. Despite this, the MARCS photospheric model reproduces, in an acceptable manner, the spectra of our sample of evolved stars in the observed CO lines. However, the predictions for the modelled angular size in CO lines, and particularly in the band head, remain largely underestimated. This reveals more extended CO layers than predicted by the MARCS photosphere model alone. Our CO-multilayer model, combined with the MARCS model, satisfactorily explains the specto-interferometric observations: the spectra, visibilities and Ψ for several kinds of evolved stars. The deduced CO temperature–density distributions are equal to, or greater than, the uppermost layer of the photospheres. Therefore, some heating mechanisms should exist in the outer atmospheres of the evolved stars, which requires further investigation.

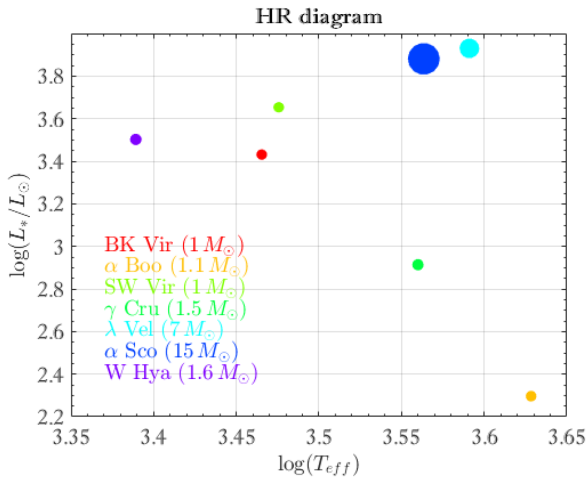

Figure 5. H–R diagram of all evolved stars studied in this work, where the symbol size of each star is proportional to its mass.

While every star is unique, our results reveal that the different types of evolved stars present, in general, the same temperature–density distributions for their spectral type. Indeed, our PAMPERO model, with its continuous and multilayer MOLsphere approach, shows the following.

(i) The RSG Antares presents a convective MOLsphere directly after its convective photosphere, from $1.06R_\star$ to $1.76R_\star$, with a highest $T_{mol} = 2350$–1900 K combined with a lower $N_{CO} = 10^{21.5}$–$10^{19.2}$ mol cm^{-2}.

(ii) The RGB stars α Boo and γ Cru and the K giant λ Vel (confirming the result of Kiss & Bedding 2003, that λ Vel is more RGB than AGB) present an important gap between the outer photosphere and the inner MOLsphere of 2.5–5.0 $R_\star$ with a size of 0.1–0.5 $R_\star$ for $T_{mol} \sim 2000$–1000 K and $N_{CO} \sim 10^{21.5}$–10^{17} mol cm^{-2}.

(iii) The normal M giants BK Vir and SW Vir, which may have a small gap between the outer photosphere and the inner MOLsphere of $\sim 0.05R_\star$, have a MOLsphere with a large size of 2–3 $R_\star$ for $T_{mol} \sim 2000$–1500 K and $N_{CO} \sim 10^{22.5}$–10^{10} mol cm^{-2}.

(iv) The Mira variable star, W Hya, presents a moderate gap between the outer photosphere and the inner MOLsphere of ∼0.2–$0.3R_\star$ with a size of $\sim 0.4R_\star$ for $T_{mol} \sim 2000$–1500 K and a rich $N_{CO} \sim 10^{22.7}$–$10^{21.5}$ mol cm^{-2}.

Fig. 5 summarizes the H–R diagram according to stellar mass of all our targets while the last part of Table B1 recaps the best six

free parameters (i.e. T_0, N_0, ζ_T, ζ_N, $R_{mol,0}$ and $R_{mol,end}$), combined with their associated uncertainties from our modelling of the eight evolved stars.

We have demonstrated that our continuous and multilayer MOLsphere approach can be used to study a large panel of evolved stars and that bi-layer MOLspheric models could be misleading, especially in the case of an observed continuous MOLsphere. Indeed, our multilayer model is a refinement of previous bi-layer models. In this work, we studied only the temperature–density distribution of the CO molecule observed by VLTI/AMBER. However, using other instruments such as CHARA/VEGA, we will be able to study the titanium monoxide (TiO) spectral lines, not only for regular evolved stars but also for yellow hyper giants. This would also allow us to study MOLspheric temperature–density distributions for other molecules such as water vapour (H_20) and silicon monoxide (SiO), simultaneously with the CO molecule. A MOLspheric temperature–density study of dust around evolved stars, especially in the *L*, *M* and *N* bands with the new instrument VLTI/MATISSE (Lopez et al. 2014) would also be very interesting. For future work, we would use the Markov chain Monte Carlo (MCMC) method on the free parameters and their uncertainties for our PAMPERO model (as we did in Hadjara et al. 2018). Prior to this, we first have to find a technical solution for how to efficiently use the MCMC method for large intervals of the six free parameters within reasonable calculation times. An eventual solution is to develop a global optimizer, which is a hybrid between the MCMC method and a genetic algorithm, called the genetic evolution Markov chain (GEMC) method (e.g. Tregloan-Reed, Southworth & Tappert 2013; Tregloan-Reed et al. 2015).

In addition to reinforcing the fact that AMBER observations with high-spectral resolution are efficient to constrain the physical properties of the outer atmosphere of cool evolved stars, this work strengthens support for the existence of some heating mechanism in the outer atmosphere of AGBs, RGBs and RSGs. We show that evolved stars deserve further study using IR spectro-interferometry. We advocate for a large survey of these stars, at different wavelengths and using a richer (u, v)-coverage, for different ranges of temperatures and luminosities. This would help us to understand better the mass-loss mechanism of the large family of evolved stars.

ACKNOWLEDGEMENTS

Based on observations performed at the European Southern Observatory (ESO), Chile under ESO AMBER Visitor mode programme IDs 081.D-0233(A), 092.D-0461(A) and 093.D-0468(A). Observed and reduced data of the eight evolved stars studied in the current paper are available in electronic form at the CDS via http://cdsarc.u-strasbg.fr/viz-bin/xxxxxx/MNRAS/. This research made use of the SIMBAD database, operated at the CDS, Strasbourg, France, and of the NASA Astrophysics Data System Abstract Service. MH acknowledges support from the scientific French association PSTJ[10] for its official host agreement, and from the Lagrange and OCA for computer server support. This research made use of the Jean-Marie Mariotti Center `SearchCal` service[11] co-developed by Lagrange and IPAG, and of the CDS Astronomical Databases SIMBAD and VIZIER.[12] This research also made use of the AMBER data reduction package of the Jean-Marie Mariotti Center.[13] Special thanks go to the project's grant ALMA-CONICYT N° 31150002 and the PI, Keiichi Ohnaka, whose work inspired our new approach to the present work. We are also grateful for the project grant ESO-MIXTO 2019, project grant QUIMAL N° 3170082, as well as grants from the Fizeau European interferometry initiative (I2E). Finally, MH and CN would like to express their warm thanks to Jeremy Tregloan-Reed (University of Antofagasta, Chile) for the help he provided for the correction of the English text of Sections 5 and 6.

[10]http://www.pstj.fr/.
[11]Available at http://www.jmmc.fr/searchcal.
[12]Available at http://cdsweb.u-strasbg.fr/.
[13]Available at http://www.jmmc.fr/amberdrs.

REFERENCES

Airapetian V., Carpenter K. G., Ofman L., 2010, ApJ, 723, 1210
Alvarez R., Plez B., 1998, A&A, 330, 1109
Arroyo-Torres B. et al., 2015, A&A, 575, A50
Ayres T. R., Brown A., Harper G. M., 2003, ApJ, 598, 610
Bertelli G., Girardi L., Marigo P., Nasi E., 2008, A&A, 484, 815
Bessell M. S., Scholz M., Wood P. R., 1996, A&A, 307, 481
Bourges L., Mella G., Lafrasse S., Duvert G., Chelli A., Le Bouquin J.-B., Delfosse X., Chesneau O., 2017, VizieR Online Data Catalog, 2346
Carpenter K. G., Robinson R. D., Harper G. M., Bennett P. D., Brown A., Mullan D. J., 1999, ApJ, 521, 382
Castelli F., Kurucz R. L., 2003, in Piskunov N., Weiss W. W., Gray D. F., eds, Proc. IAU Symp. 210, Modelling of Stellar Atmospheres. Kluwer, Dordrecht, p. A20
Chelli A., Utrera O. H., Duvert G., 2009, A&A, 502, 705
Chiavassa A., Haubois X., Young J. S., Plez B., Josselin E., Perrin G., Freytag B., 2010, A&A, 515, A12
Chiavassa A. et al., 2011, A&A, 528, A120
Cruzalèbes P., Jorissen A., Chiavassa A., Paladini C., Rabbia Y., Spang A., 2015, MNRAS, 446, 3277
De Beck E., Decin L., de Koter A., Justtanont K., Verhoelst T., Kemper F., Menten K. M., 2010, A&A, 523, A18
De Beck E., Decin L., Ramstedt S., Olofsson H., Menten K. M., Patel N. A., Vlemmings W. H. T., 2017, A&A, 598, A53
Decin L., Vandenbussche B., Waelkens C., Decin G., Eriksson K., Gustafsson B., Plez B., Sauval A. J., 2003, A&A, 400, 709
Di Criscienzo M. et al., 2016, MNRAS, 462, 395
Dijkstra C., Speck A. K., 2006, ApJ, 651, 288
Ducati J. R., 2002, VizieR Online Data Catalog, 2237
Edlén B., 1966, Metrologia, 2, 71
Famaey B., Pourbaix D., Frankowski A., van Eck S., Mayor M., Udry S., Jorissen A., 2009, A&A, 498, 627
García-Hernández D. A., García-Lario P., Plez B., Manchado A., D'Antona F., Lub J., Habing H., 2007, A&A, 462, 711
Gontcharov G. A., 2006, Astron. Lett., 32, 759
González Delgado D., Olofsson H., Kerschbaum F., Schöier F. L., Lindqvist M., Groenewegen M. A. T., 2003, A&A, 411, 123
Goorvitch D., 1994, ApJS, 95, 535
Guha Niyogi S., Speck A. K., Volk K., 2011, The Astronomical Review, 6, 27
Gustafsson B., Edvardsson B., Eriksson K., Jørgensen U. G., Nordlund Å., Plez B., 2008, A&A, 486, 951
Habing H. J., 1996, A&AR, 7, 97
Hadjara M., 2015, PhD thesis. Université de Sophia Antipolis
Hadjara M. et al., 2014, A&A, 569, A45
Hadjara M., Petrov R. G., Jankov S., Cruzalèbes P., Spang A., Lagarde S., 2018, MNRAS, 480, 1263
Haubois X. et al., 2009, A&A, 508, 923
Hinkle K. H., Scharlach W. W. G., Hall D. N. B., 1984, ApJS, 56, 1
Höfner S., Olofsson H., 2018, A&AR, 26, 1
Ireland M. J., Scholz M., Wood P. R., 2011, MNRAS, 418, 114
Ita Y. et al., 2007, PASJ, 59, S437

Jankov S., Vakili F., Domiciano de Souza A., Jr., Janot-Pacheco E., 2001, A&A, 377, 721
Kervella P., Thévenin F., Ségransan D., Berthomieu G., Lopez B., Morel P., Provost J., 2003, A&A, 404, 1087
Kiss L. L., Bedding T. R., 2003, MNRAS, 343, L79
Knapp G. R., Young K., Lee E., Jorissen A., 1998, ApJS, 117, 209
Knapp G. R., Pourbaix D., Platais I., Jorissen A., 2003, A&A, 403, 993
Kurucz R. L., 2005, Memorie della Societa Astronomica Italiana Supplementi, 8, 14
Labeyrie A., Koechlin L., Bonneau D., Blazit A., Foy R., 1977, ApJ, 218, L75
Lebzelter T., Kerschbaum F., Hron J., 1995, A&A, 298, 159
Léger A., Defrère D., Malbet F., Labadie L., Absil O., 2015, ApJ, 808, 194
Li X., Millar T. J., Heays A. N., Walsh C., van Dishoeck E. F., Cherchneff I., 2016, A&A, 588, A4
Lopez B. et al., 2014, The Messenger, 157, 5
Luck R. E., 2014, AJ, 147, 137
Mangum J. G., Shirley Y. L., 2015, PASP, 127, 266
Martí-Vidal I., Marcaide J. M., Quirrenbach A., Ohnaka K., Guirado J. C., Wittkowski M., 2011, A&A, 529, A115
Meinel A. B., Meinel M. P., 1977, NASA STI/Recon Technical Report A, 77,
Mérand A., Patru F., Berger J.-P., Percheron I., Poupar S., 2012, in Delplancke F. , Rajagopal J. K., Malbet F., eds, Proc. SPIE 8445, Optical and Infrared Interferometry III. SPIE, Bellingham, WA, p. 84451K
Miguel M., 2014, PhD thesis. Université Pierre et Marie Curie (Paris VI)
Millour F. et al., 2007, A&A, 464, 107
Mondal S., Chandrasekhar T., 2005, AJ, 130, 842
Montargès M., Kervella P., Perrin G., Ohnaka K., Chiavassa A., Ridgway S. T., Lacour S., 2014, A&A, 572, A17
Niyogi S. G., Speck A. K., Volk K., 2011, The Astronomical Review, 6, 27
Ohnaka K., 2004, A&A, 421, 1149
Ohnaka K., 2013, A&A, 553, A3
Ohnaka K., 2014, A&A, 561, A47
Ohnaka K., Morales Marín C. A. L., 2018, A&A, 620, A23
Ohnaka K. et al., 2009, A&A, 503, 183
Ohnaka K. et al., 2011, A&A, 529, A163
Ohnaka K., Hofmann K.-H., Schertl D., Weigelt G., Malbet F., Massi F., Meilland A., Stee P., 2012, A&A, 537, A53
Ohnaka K., Hofmann K.-H., Schertl D., Weigelt G., Baffa C., Chelli A., Petrov R., Robbe-Dubois S., 2013, A&A, 555, A24
Ohnaka K., Weigelt G., Hofmann K.-H., 2016, A&A, 589, A91
Ohnaka K., Weigelt G., Hofmann K.-H., 2017a, Nature, 548, 310
Ohnaka K., Weigelt G., Hofmann K.-H., 2017b, A&A, 597, A20
Ohnaka K., Hadjara M., Maluenda Berna M. Y. L., 2019, A&A, 621, A6
Origlia L., Rood R. T., Fabbri S., Ferraro F. R., Fusi Pecci F., Rich R. M., 2007, ApJ, 667, L85
Origlia L., Rood R. T., Fabbri S., Ferraro F. R., Fusi Pecci F., Rich R. M., Dalessandro E., 2010, ApJ, 718, 522
Origlia L., Ferraro F. R., Fabbri S., Fusi Pecci F., Dalessandro E., Rich R. M., Valenti E., 2014, A&A, 564, A136
Perrin G., Ridgway S. T., Coudé du Foresto V., Mennesson B., Traub W. A., Lacasse M. G., 2004, A&A, 418, 675
Petrov R. G. et al., 2007, A&A, 464, 1
Plez B., 2012, Turbospectrum: Code for spectral synthesis, Astrophysics Source Code Library (ascl:1205.004)
Ramstedt S., Olofsson H., 2014, A&A, 566, A145
Richichi A., Percheron I., 2005, VizieR Online Data Catalog, 343,
Richichi A., Percheron I., Khristoforova M., 2005, A&A, 431, 773
Samus' N. N., Kazarovets E. V., Durlevich O. V., Kireeva N. N., Pastukhova E. N., 2017, Astronomy Reports, 61, 80
Schwarzschild M., 1975, ApJ, 195, 137
Suzuki T. K., 2007, ApJ, 659, 1592
Tatulli E. et al., 2007, A&A, 464, 29
Tregloan-Reed J., Southworth J., Tappert C., 2013, MNRAS, 428, 3671
Tregloan-Reed J. et al., 2015, MNRAS, 450, 1760
Tsuji T., 2001, A&A, 376, L1
Tsuji T., 2006, ApJ, 645, 1448
Tsuji T., Ohnaka K., Aoki W., Yamamura I., 1997, A&A, 320, L1
van Cittert P. H., 1934, Physica, 1, 201
van Leeuwen F., 2007, A&A, 474, 653
Wachter A., Schröder K.-P., Winters J. M., Arndt T. U., Sedlmayr E., 2002, A&A, 384, 452
Wallace L., Hinkle K., 1996, ApJS, 107, 312
Winters J. M., Le Bertre T., Jeong K. S., Nyman L.-Å., Epchtein N., 2003, A&A, 409, 715
Wittkowski M., Boboltz D. A., Ohnaka K., Driebe T., Scholz M., 2007, A&A, 470, 191
Wittkowski M., Chiavassa A., Freytag B., Scholz M., Höfner S., Karovicova I., Whitelock P. A., 2016, A&A, 587, A12
Wittkowski M. et al., 2017, A&A, 601, A3
Woolf N. J., 1973, in Greenberg J. M., van de Hulst H. C., eds, Proc. IAU Symp. 52, Interstellar Dust and Related Topics, Kluwer, Dordrecht, p. 485
Zernike F., 1938, Physica, 5, 785

APPENDIX A: DATA INTERPRETATION FIGURES

We gather here all the figures of the data interpretation section (Section 3) for γ Cru, λ Vel, α Sco and W Hya (phases 0.59 and 0.77), respectively.

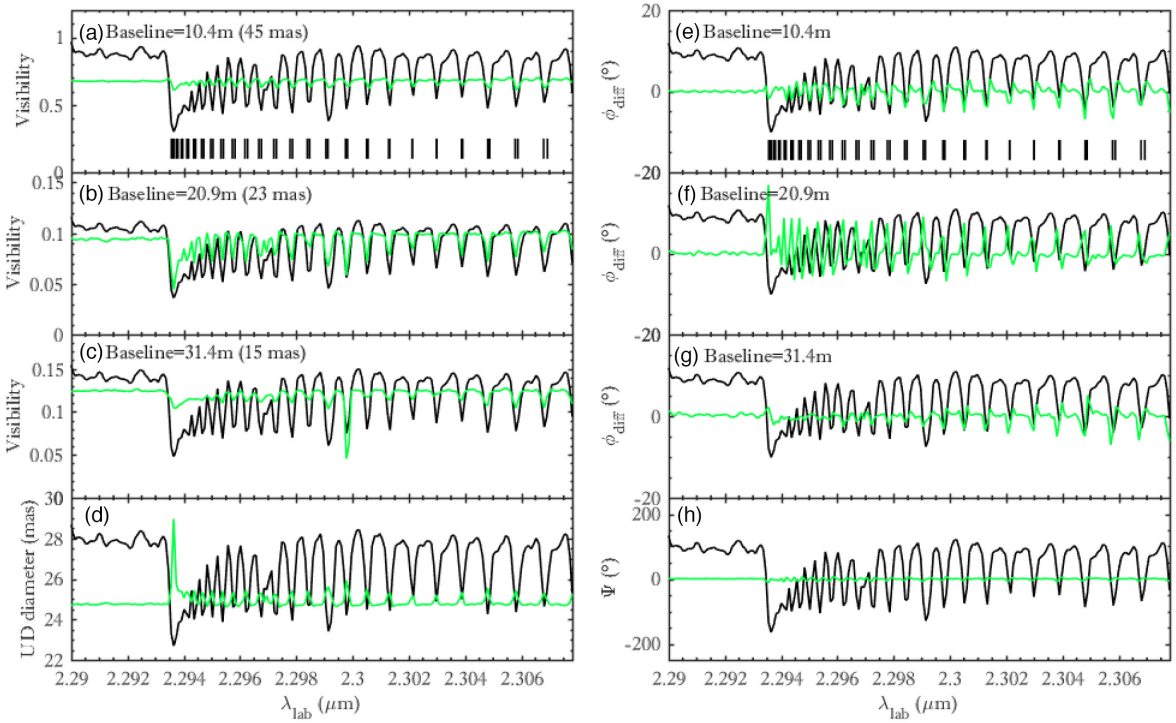

Figure A1. AMBER data of γ Cru. In each panel, the scaled observed spectrum is plotted by black solid lines. (a)–(c) Visibilities observed on the reported triplet baselines are shown (coloured lines), and the corresponding spatial resolutions are also given. (d) Uniform-disc diameter (coloured line) derived by fitting the visibilities shown in panels (a)–(c). (e)–(g) Differential phases ($\phi_{\rm diff}$) observed on the reported triplet baselines are shown (coloured lines). (h) Closure phase (Ψ) shown as a coloured line.

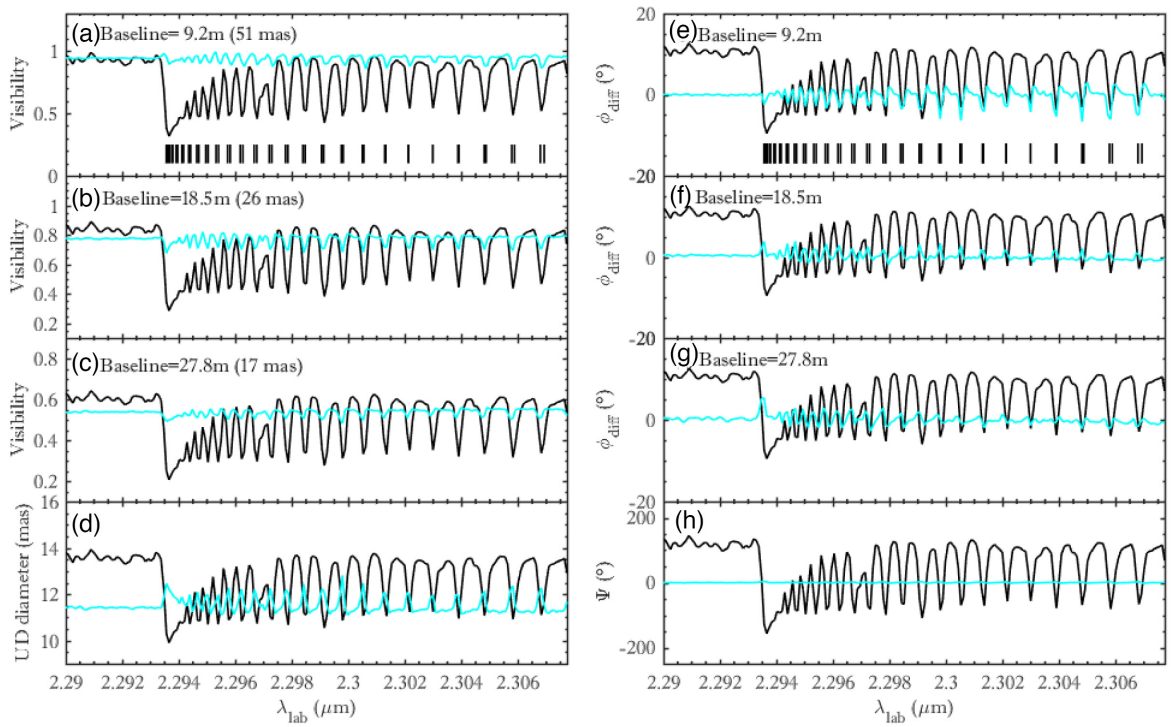

Figure A2. Same as Fig. A1 for λ Vel.

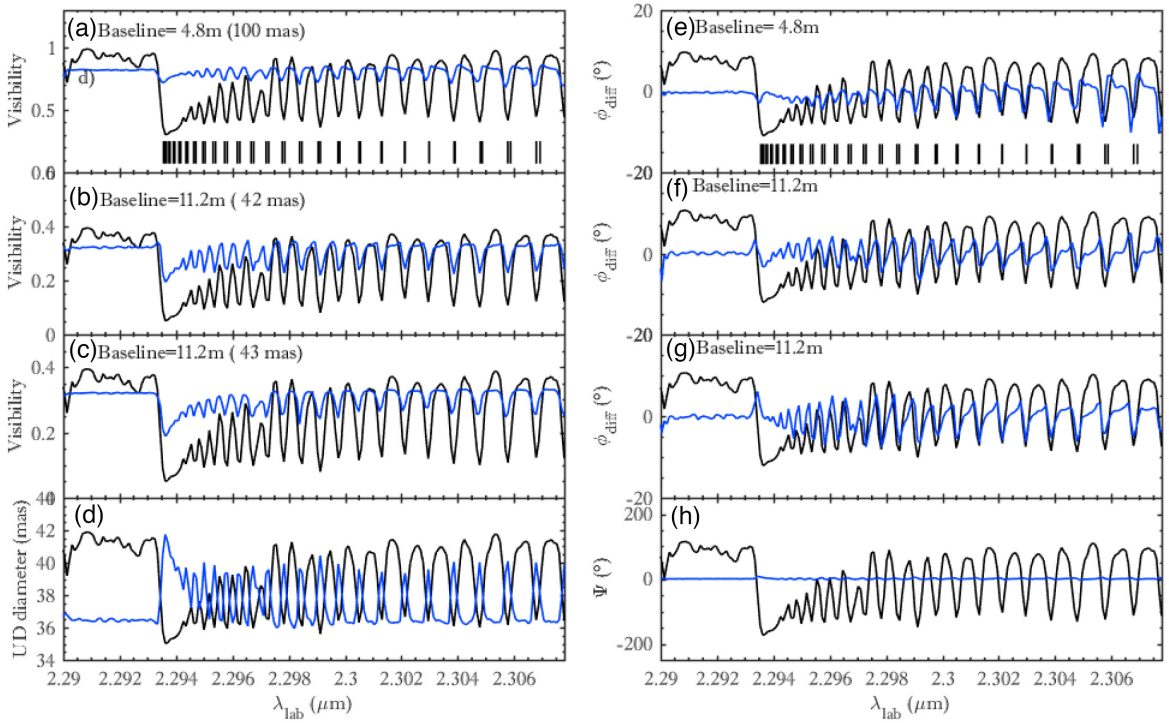

Figure A3. Same as Fig. A1 for α Sco.

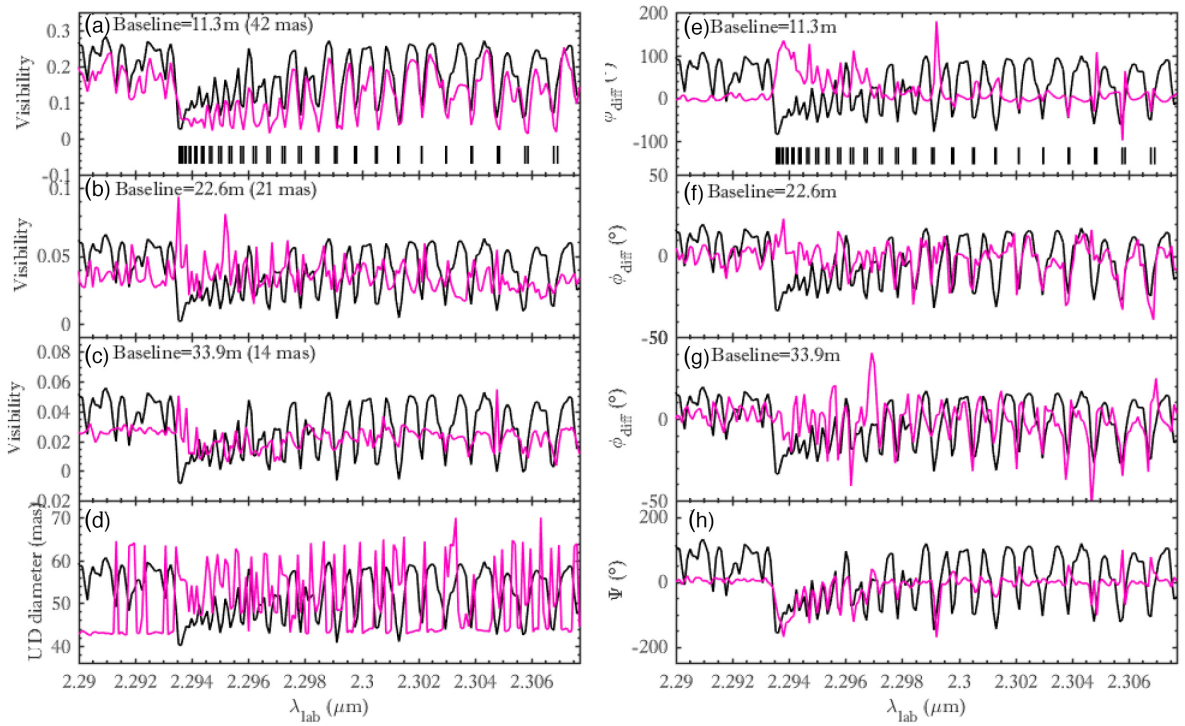

Figure A4. Same as Fig. A1 for W Hya (phase 0.59).

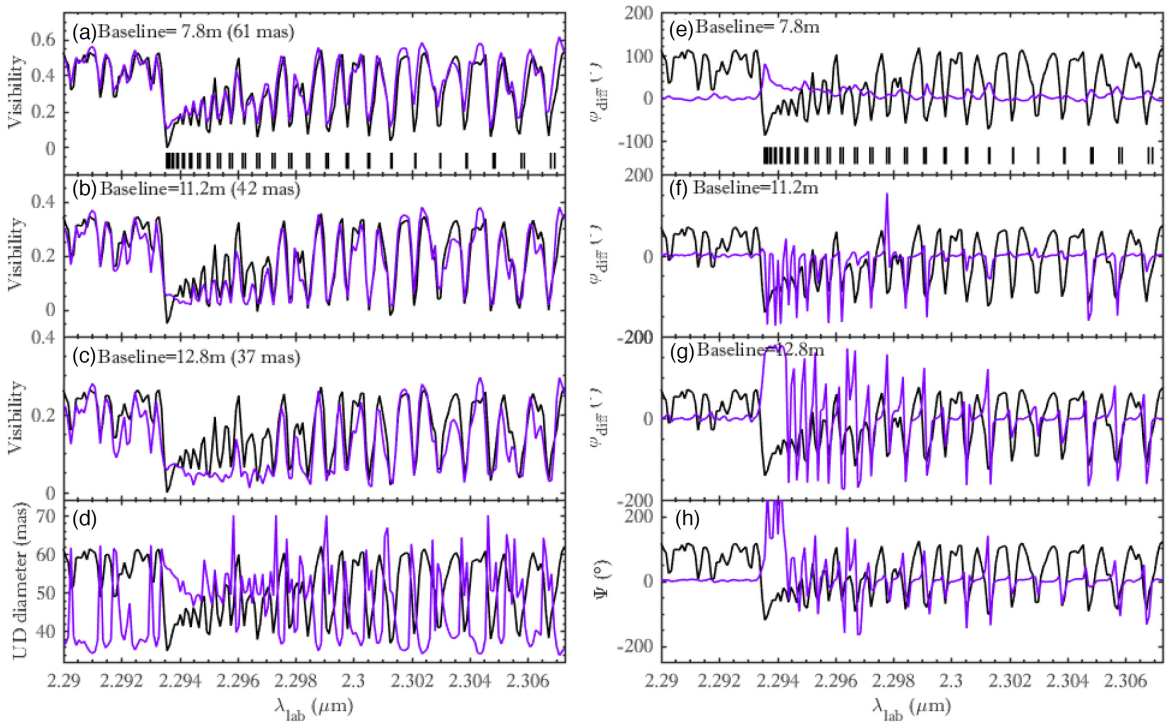

Figure A5. Same as Fig. A1 for W Hya (phase 0.77).

APPENDIX B: PARAMETERS OF STELLAR ATMOSPHERE MODELS AND MOLSPHERE'S RESULTS

In Table B1, we summarize the basic stellar parameters, the chosen MARCS models and the best six free parameters with their uncertainties of PAMPERO for our sample of eight evolved stars, where we compare old published results of BK Vir, α Boo and SW Vir (using a MARCS + two-layer model) with our results (using PAMPERO). Note that PAMPERO works also with two layers and it gives the same results that are found in the literature, with negligible differences, as shown in Figs D1–D3.

Table B1. Basic stellar parameters, chosen MARCS models and the best six free parameters – see Ohnaka et al. (2012), Ohnaka & Morales Marín (2018) and Ohnaka et al. (2019), and references therein, for BK Vir, α Boo and SW Vir, respectively – with their uncertainties of PAMPERO for our sample of evolved stars. Because of the similarity in $T_{\rm eff}$, log g and $M_\star$ between α Orionis and α Scorpii, according to Ohnaka (2013), we adopt the same chemical composition for α Sco as that of α Ori.

Star	BK Vir	α Boo	SW Vir	γ Cru	λ Vel	α Sco	W Hya	
Spectral type	M7 III (AGB)	K1.5 III (RGB)	M7 III (AGB)	M3.5 III (RGB)	K4 Ib (RGB/AGB)	M1.5 Ib (RSG)	M7.5 e (Mira)	
Variability type[a]	SRB	No	SRB	No	LC	LC	SRA	
Magnitude (V)[a]	7.28–8.8	-0.05^b	6.40–7.90	1.64^b	2.14–2.30	0.88–1.16	7.7–11.6	
Distance (pc)[c]	181^{+25}_{-20}	11.26 ± 0.07	143^{+19}_{-15}	27.15 ± 0.13	167 ± 3	$169.78^{+34.72}_{-24.64}$	$78^{+6.5}_{-5.6}{}^d$	
$\varnothing_\star$ (mas)	10.73 ± 0.23	20.4 ± 0.2	16.23 ± 0.20	24.70 ± 0.35	11.1 ± 0.8	37.61 ± 0.12	46.6 ± 0.1	
$T_{\rm eff}$ (K)	2920 ± 150	4250 ± 50	2990 ± 50	3630 ± 90	3800–4000	3660 ± 120	2400–2500	
log g (cm s^{-2})	~ -0.17	$+1.7 \pm 0.1$	-0.3 ± 0.1	$+0.9 \pm 0.1$	$+0.64$	-0.2 ± 0.3	-0.86 ± 0.17^e	
$M_\star$ (M$_\odot$)	~ 1	~ 1.1	1–1.25	1.5 ± 0.3	7 ± 1	15 ± 5	1.6 ± 0.4^e	
$L_\star$ (L$_\odot$)	2700 ± 850	198 ± 3	4500 ± 1100	820 ± 80	8511 ± 982	7600^{+5300}_{-3100}	3180^{+550}_{-440}	
$v_{\rm micro}$ (km s^{-1})	3–4 (no solar)	~ 2 (solar)	~ 4 (no solar)	~ 2 (solar)	~ 2 (solar)	~ 5 (no solar)	3–4 (no solar)	
[Fe/H]	~ 0.0 (solar)	-0.5 (no solar)	~ 0.0 (solar)	~ 0.0 (solar)	0.06 (solar)	~ 0.0 (solar)	0.78^e (no solar)	
Chemical composition	C/N 1.5	^{12}C/^{13}C 7 ± 2^f	^{12}CO/^{13}CO 18^g	^{12}CO/^{13}CO ~ 20	C/O $\sim 0.9^h$	N/O $\sim 1^i$	^{12}CO/^{13}CO 10^g	
Reference (see also references therein)	Ohnaka et al. (2012)	Ohnaka & Morales Marín (2018); Ohnaka (2014)	Ohnaka et al. (2019)	Ohnaka (2014)	Carpenter et al. (1999)	Ohnaka (2014); Ohnaka et al. (2013,2017a)	Ohnaka et al. (2016, 2017b)	
MARCS model								
$T_{\rm eff}$	3000	4250	3000	3600	4000	3600	2500	
log g	0.0	1.5	0.0	1.0	1.0	0.0	0.0	
$M_\star$	1.0	1.0	1.0	1.0	5.0	5.0	1.0	
$v_{\rm micro}$	2.0	2.0	2.0	2.0	2.0	5.0	2.0	
[Fe/H]	+0.0	–0.5	+0.0	+0.0	+0.0	+0.0	+0.25	
CN-cycled composition	Moderately	Moderately	Moderately	Moderately	Moderately	Heavily	Heavily	
In the literature: MARCS + two-layer MOLsphere models, with 0.1$R_\star$ of thickness								
$R_{\rm inner}$ ($R_\star$)	1.2–1.25	1.04 ± 0.02	1.3 ± 0.1	–	–	–	–	–
$R_{\rm outer}$ ($R_\star$)	2.5–3.0	2.6 ± 0.2	2.0 ± 0.2	–	–	–	–	–
$T_{\rm inner}$ (K)	1900–2100	1600 ± 400	2000 ± 100	–	–	–	–	–
$T_{\rm outer}$ (K)	1500–2100	1800 ± 100	1700 ± 100	–	–	–	–	–
$N_{\rm CO,\,inner}$ (mol cm^{-2})	$(1–2) \times 10^{22}$	$10^{20 \pm 0.3}$	$10^{22 \pm 0.3}$	–	–	–	–	–
$N_{\rm CO,\,outer}$ (mol cm^{-2})	$10^{19}-10^{20}$	$10^{19 \pm 0.15}$	$10^{20 \pm 0.6}$	–	–	–	–	–
MARCS + PAMPERO models (thickness $= 0.1R_\star$)								
Luminosity phase	–	–	–	–	–	–	0.59	0.77
$\boldsymbol{R}_{\rm mol,0}$ ($R_\star$)	1.2 ± 0.2	2.5 ± 0.2	1.2 ± 0.1	5.15 ± 0.1	4.5 ± 0.1	$1.06^{+0.05}_{-0.0}$	1.3 ± 0.05	1.4 ± 0.05
$\boldsymbol{R}_{\rm mol,end}$ ($R_\star$)	4.5 ± 0.2	3.0 ± 0.2	3.0 ± 0.2	5.25 ± 0.1	5.0 ± 0.1	1.76 ± 0.05	1.7 ± 0.05	1.8 ± 0.05
$\boldsymbol{T}_0$ (K)	2010 ± 50	1650 ± 30	1950 ± 50	960 ± 40	1000 ± 50	2350 ± 50	1950 ± 50	2000 ± 50
$\boldsymbol{\zeta}_{\rm T}$	0.35 ± 0.2	6.56 ± 0.50	0.06 ± 0.05	0.10 ± 0.05	0.10 ± 0.05	1 ± 0.1	0.60 ± 0.05	0.60 ± 0.05
$\boldsymbol{N}_0$ (mol/cm^{-2})	$10^{22.3} \pm 10^{0.2}$	$10^{19.2} \pm 10^{0.1}$	$10^{22.5} \pm 10^{0.2}$	$10^{21.5} \pm 10^{0.2}$	$10^{21.5} \pm 10^{0.2}$	$10^{21.5} \pm 10^{0.2}$	$10^{22.7} \pm 10^{0.2}$	$10^{22.7} \pm 10^{0.2}$
$\boldsymbol{\zeta}_{\rm N}$	18 ± 3	30 ± 5	30 ± 5	50 ± 5	50 ± 5	35 ± 5	10 ± 3	10 ± 3
Number of layers	33	5	18	1	5	7	4	4

[a] Taken from the GCVS, version 5.1 (Samus' et al. 2017), unless otherwise stated. [b] Taken from Ducati (2002). [c] Taken from van Leeuwen (2007), unless otherwise stated. [d] Taken from Knapp et al. (2003). [e] Our estimation using the theoretical evolutionary tracks of Bertelli et al. (2008).
[f] Taken from Decin et al. (2003) with CNO abundances of 7.96 ± 0.20, 7.61 ± 0.25 and 8.68 ± 0.20 dex, respectively.
[g] Taken from Ramstedt & Olofsson (2014).
[h] Taken from Luck (2014).
[i] Taken from Tsuji (2006) with CNO abundances of ~ 8, ~ 8.5 and 8.5 dex, respectively.

APPENDIX C: MARCS+PAMPERO MODELS GRIDS AND χ^2 RESTRICTED MINIMIZATION INTERVALS

In Table C1, we summarize the huge grids of THE MARCS+PAMPERO models and the χ^2 restricted minimization intervals that we used to determine our best results (the last panel of Table B1).

Table C1. MARCS+PAMPERO model grids and χ^2 restricted minimization intervals. The paths of our six free parameters are $\Delta R = 0.2R_\star$ for $R_{\rm mol,0}$ and $\Delta R = 0.5R_\star$ for $R_{\rm mol,end}$, $\Delta T = 100$ K for T_0, $\Delta N = 10^{0.3}$ mol cm^{-2} for N_0, $\Delta\zeta_{\rm T} = 1$ and $\Delta\zeta_{\rm N} = 10$.

Star	BK Vir	α Boo	SW Vir	γ Cru	λ Vel	α Sco	W Hya
MARCS+PAMPERO models: grids							
$R_{\rm mol,0}$ ($R_\star$)	1.2–1.6	1.05–3.05	1.2–1.6	1.04–5.64	1.02–5.02	1.06–1.66	1.15–1.55
$R_{\rm mol,end}$ ($R_\star$)	1.3–5.6	1.1–4.1	1.3–4.3	1.2–6.2	1.2–6.2	1.2–3.2	1.2–3.2
T_0 (K)	1900–2200	1500–2500	1900–2200	900–2500	900–2500	1900–2500	1800–2500
$\zeta_{\rm T}$	0.01–5.01	0.01–10.01	0.01–5.01	0.01–5.01	0.01–5.01	0.01–5.01	0.01–5.01
N_0 (mol cm^{-2})	10^{21-23}	10^{18-23}	10^{21-23}	10^{18-23}	10^{18-23}	10^{21-23}	10^{21-23}
$\zeta_{\rm N}$	5–25	5–45	5–45	5–65	5–65	5–45	5–25
Number of grids	1	3	1	3	3	1	1
Number of models	~6500	~6500 × 3	~8600	~12 000 × 3	~12 000 × 3	~21 000	~17 000
Calculation time	~60h	~180h	~72h	~300h	~300h	180h	~150h
MARCS+PAMPERO models: χ^2 restricted minimization intervals							
$R_{\rm mol,0}$ ($R_\star$)	1.2–1.3	2–3	1.2–1.3	4.5–5.5	4–5	1.06–1.5	1.25–1.45
$R_{\rm mol,end}$ ($R_\star$)	3–5	2–5	2–5	5–6	4.5–5.5	1.5–2	1.5–2
T_0 (K)	1900–2100	1500–1800	1900–2100	900–1200	900–1200	2200–2500	1900–2100
$\zeta_{\rm T}$	0.1–1	5–10	0.01–0.1	0.05–0.5	0.05–0.5	0.5–1.5	0.1–1
N_0 (mol cm^{-2})	10^{22-23}	10^{19-20}	10^{22-23}	10^{21-22}	10^{21-22}	10^{21-22}	10^{22-23}
$\zeta_{\rm N}$	15–25	20–40	20–40	45–55	45–55	30–40	5–15
Calculation time	~72h	~72h	~72h	~72h	~72h	~72h	~72h × 2

APPENDIX D: FIGURES OF THE RESULTS SECTION

We gather here all the figures of the results section (Section 5) for BK Vir, α Boo, SW Vir, γ Cru, λ Vel, α Sco and W Hya (phases 0.59 and 0.77), respectively.

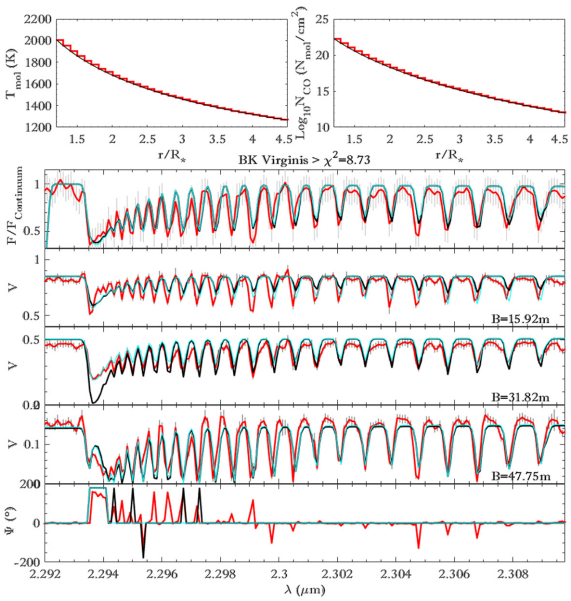

Figure D1. Our best-fitting PAMPERO model for BK Vir. Top: MOLsphere's temperature ($T_{\rm mol}$) and CO column density ($N_{\rm CO}$) distributions along the stellar radius ($r/R_\star$) respectively (layer-by-layer in coloured stepped lines with the global behaviour in black lines). Bottom: Spectro-interferometric comparisons between the observations (the coloured line used in the top panel) and our best model (black line), for the normalized flux $F/F_{\rm Continuum}(\lambda)$, the visibilities $V(\lambda)$ for their respective baselines (B) and closure phase $\Psi(\lambda)$. In another colour, we show the best bi-layer result (of Table B1).

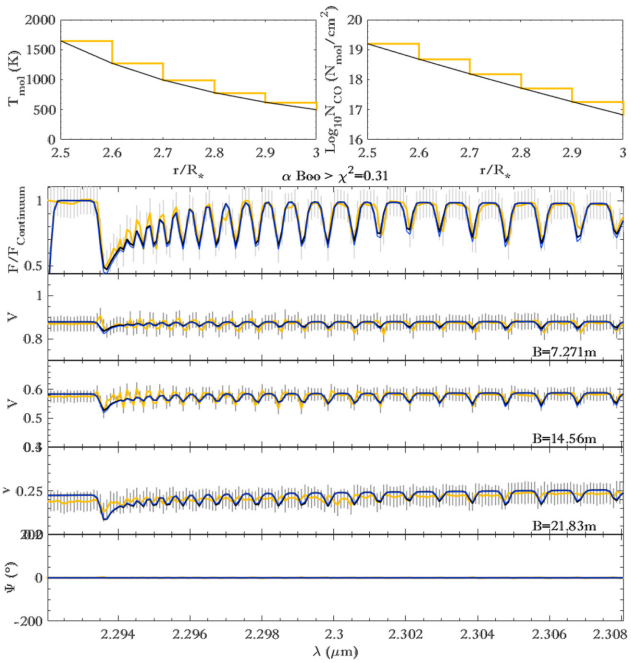

Figure D2. Our best-fitting PAMPERO model for α Boo (see caption for Fig. D1).

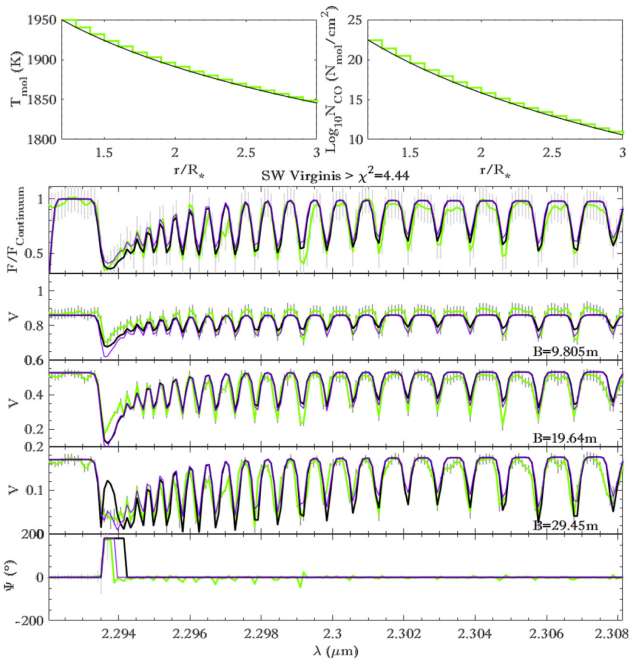

Figure D3. Our best-fitting PAMPERO model for SW Vir (see caption for Fig. D1).

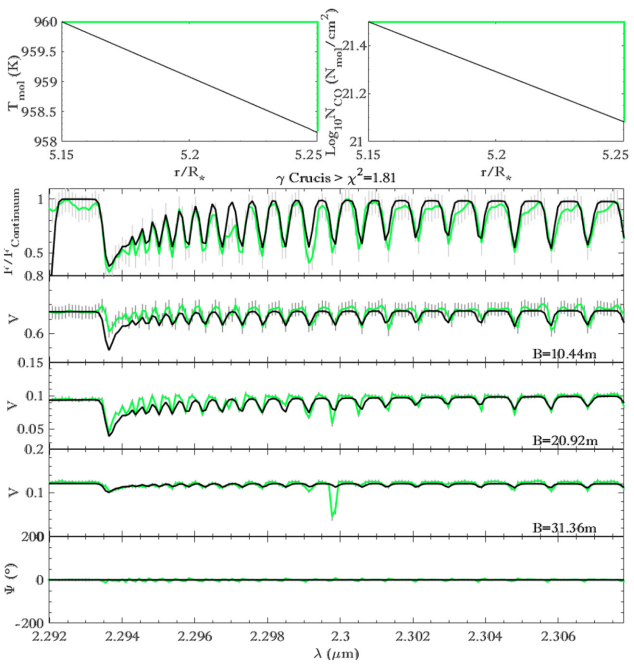

Figure D4. Our best-fitting PAMPERO model for γ Cru (see caption for Fig. D1).

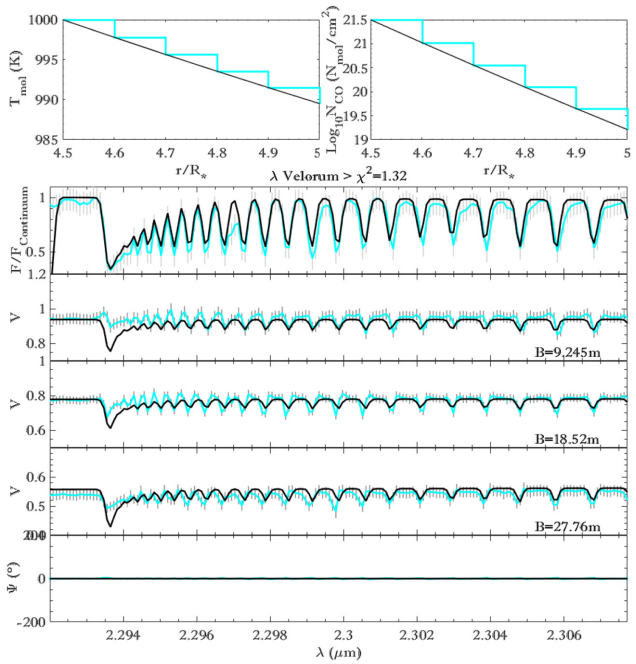

Figure D5. Our best-fitting PAMPERO model for λ Vel (see caption for Fig. D1).

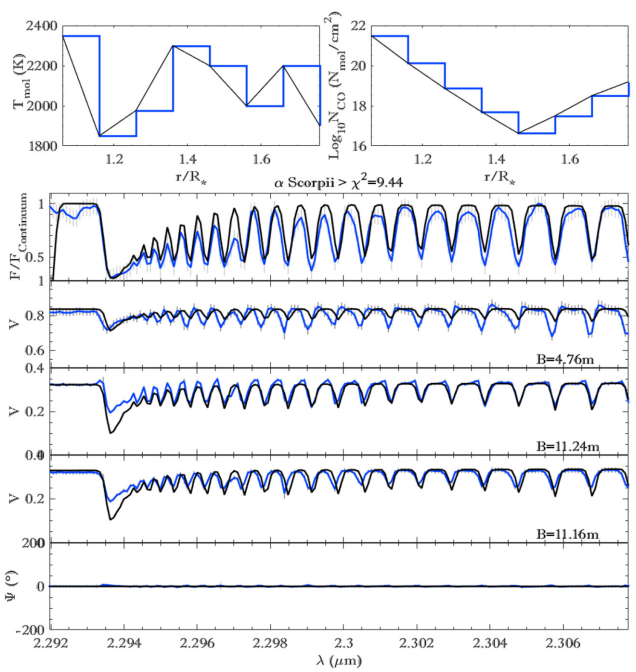

Figure D6. Our best-fitting PAMPERO model for α Sco (see caption for Fig. D1).

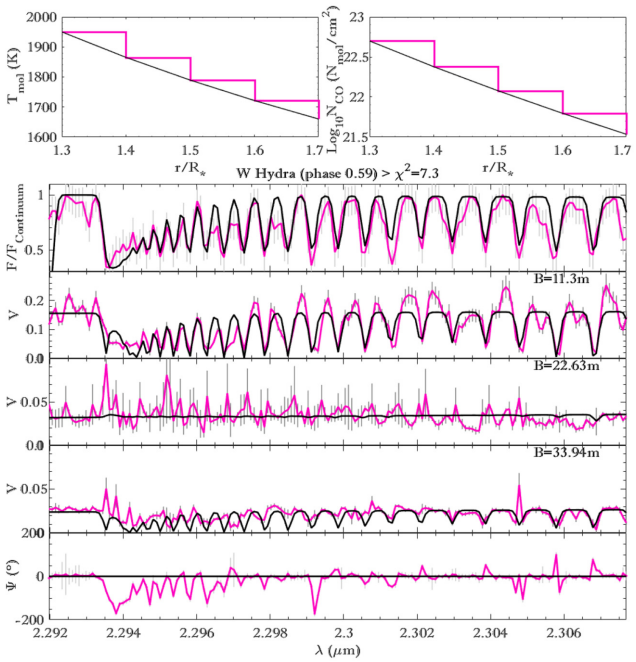

Figure D7. Our best-fitting PAMPERO model for W Hya at phase 0.59 (see caption for Fig. D1).

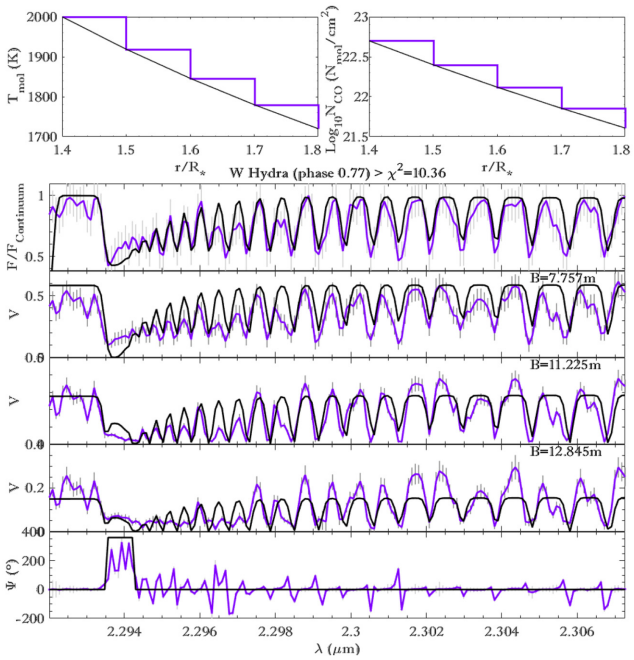

Figure D8. Our best-fitting PAMPERO model for W Hya at phase 0.77 (see caption for Fig. D1).

This paper has been typeset from a TEX/LATEX file prepared by the author.